JM PAPERS

Dynamics of a viscoelastic thread surrounded by a Newtonian viscous fluid inside a cylindrical tube

Fang Li[1] and Dongdong He[2],†

[1]Department of Modern Mechanics, University of Science and Technology of China, Hefei, Anhui 230027, PR China

[2]School of Science and Engineering, The Chinese University of Hong Kong, Shenzhen, Guangdong 518172, PR China

A viscoelastic thread in vacuum is known to evolve into a beads-on-a-string structure at large deformations. If the thread is immersed in another fluid, the surrounding medium may influence the topological structure of it, which remains unexplored. To get some insights into the nonlinear behaviour of a viscoelastic thread in a two-phase flow system, a one-dimensional model is developed under the slender body approximation, in which the thread of a highly viscoelastic fluid described by the Oldroyd-B or Giesekus constitutive equation is immersed in a Newtonian viscous fluid of much smaller density and viscosity inside a cylindrical tube. The effect of the outer viscous fluid layer and the confinement of the tube is examined. It is found that the outer fluid may change substantially the beads-on-a-string structure of the viscoelastic thread. Particularly, it may induce the formation of secondary droplets on the filament between adjacent primary droplets, even for large wavenumbers. The outer fluid exerts a resistance force on the extensional flow in the filament, but the necking of the thread is slightly accelerated, due to the redistribution of capillary and elastic forces along the filament accompanied by the formation of secondary droplets. Decreasing the tube radius leads to an increase in secondary droplet size but affects little the morphology of the thread. The non-uniformity of the filament between droplets is more pronounced for a Giesekus viscoelastic thread, and pinch-off of a Giesekus thread always occurs in the neck region connecting the filament to the primary droplet in the presence of the outer viscous fluid.

Key words: nonlinear instability, core–annular flow, viscoelasticity

† Email address for correspondence: hedongdong@cuhk.edu.cn

1. Introduction

Instability and breakup of viscoelastic fluid threads or jets are frequently encountered in nature and in a variety of applications including spraying, coating, fibre spinning, ink-jet printing, medical diagnostics, rheological measurement, etc. As early as five decades ago, researchers observed that a viscoelastic jet evolves into a long-lived beads-on-a-string structure in which spheroidal droplets are connected by thin filaments of almost uniform thickness (Middleman 1965; Goldin *et al.* 1969). To date, rich dynamics of this beads-on-a-string morphology has been extensively explored. It has been found that zero, single or multiple small secondary droplets can be formed between two adjacent large primary droplets, depending on the interplay of capillary, inertial, viscous and elastic forces (Ardekani, Sharma & Mckinley 2010; Bhat *et al.* 2010; Malkin, Arinstein & Kulichikhin 2014; Turkoz *et al.* 2018*b*; Pingulkar, Peixinho & Crumeyrolle 2020). Generally, more secondary droplets tend to be formed at smaller viscosities or smaller elasticities (Bhat *et al.* 2010). In addition, initial harmonic perturbations of long wavelength favour the formation of secondary droplets (Ardekani *et al.* 2010; Li, Yin & Yin 2017*a*). In contrast to Newtonian threads, a non-Newtonian viscoelastic filament, if it is free of secondary droplets, undergoes a uniaxial extension. With continuous stretching of the filament, strain hardening comes into play, and the extensional viscosity can be several orders of magnitude greater than the zero-shear viscosity of the viscoelastic fluid, which results in extremely large elastic stresses that slow down filament thinning significantly (Feng 2003; Ardekani *et al.* 2010). An Oldroyd-B viscoelastic filament is known to neck down exponentially in time at a rate of $1/3De$, where the Deborah number $De = \lambda/t_c$ is defined as the ratio of the stress relaxation time λ to the capillary time t_c (Chang, Demekhin & Kalaidin 1999; Clasen *et al.* 2006*a*; Ardekani *et al.* 2010). Meanwhile the polymeric stress in the filament increases exponentially at the same rate. It has also been recognized that the nonlinear evolution of an Oldroyd-B viscoelastic thread profile possesses self-similar solutions (Clasen *et al.* 2006*a*; Deblais *et al.* 2020; Eggers, Herrada & Snoeijer 2020).

Recently, the blistering instability occurring in a fully stretched filament of polymer solution has drawn a lot of attention. When a uniform filament between large primary droplets gets sufficiently thin, a Rayleigh–Plateau-like instability may arise, leading to the formation of secondary droplets on the filament (Christanti & Walker 2001; Oliveira, Yeh & McKinley 2006; Sattler, Wagner & Eggers 2008; Sattler *et al.* 2012; Eggers 2014). Mechanisms have been proposed to explain this phenomenon, e.g. elastic drainage and resulting filament recoil (Chang *et al.* 1999), phase separation (pure solvent droplets are formed on a fine filament of high concentrated polymer solution) (Sattler *et al.* 2008; Eggers 2014; Kulichikhin *et al.* 2014; Deblais, Velikov & Bonn 2018) and finite extensibility of polymer chains (Malkin *et al.* 2014). For the last one, the Giesekus or finitely extensible nonlinear elastic (FENE) model is used in the corresponding theoretical description.

Based on the slender body approximation, several one-dimensional (1-D) models were built, which have proved to be able to predict morphologies of viscous or viscoelastic fluid threads at large times with reasonable accuracy and much less computation time compared with direct numerical simulations (Bousfield *et al.* 1986; Eggers & Dupont 1994; Eggers & Villermaux 2008; Tembely *et al.* 2012; Vadillo *et al.* 2012; Turkoz *et al.* 2018*a*). These 1-D models are also useful in theoretical analysis. For instance, by balancing axial polymeric stress and capillary pressure, the 1-D Oldroyd-B model predicted theoretically the $1/3De$ exponential law of filament thinning (Clasen *et al.* 2006*a*). In addition, the 1-D models were broadly used in studying self-similarity in the corner region connecting a filament to a droplet (Clasen *et al.* 2006*a*; Bhat *et al.* 2012; Mathues *et al.* 2018).

926 A21-2

The disadvantage of the 1-D models is that radial flow in droplets and off-diagonal polymeric stress components are ignored, which have been shown to become important in the later stages of filament thinning using two-dimensional (2-D) numerical simulation (Turkoz *et al.* 2018*a*). More 2-D numerical simulations of large axisymmetric deformations of viscoelastic fluid threads are expected in the future.

In the framework of the Oldroyd-B model, pinch-off of threads cannot be predicted, because of its limit of infinite extensibility. To describe the finite-time breakup of polymer threads or jets as observed in experiments, the Giesekus or FENE model is appropriate (Entov & Hinch 1997; Chang *et al.* 1999; Fontelos & Li 2004; Ardekani *et al.* 2010; Tembely *et al.* 2012; Vadillo *et al.* 2012; Wagner, Bourouiba & McKinley 2015; Snoeijer *et al.* 2020). These two models, especially the latter, are quite favourable in experimental data fitting as well (Entov & Hinch 1997; Anna & McKinley 2001; Tembely *et al.* 2012). In the Giesekus model, the so-called mobility factor α, which is associated with the anisotropy of hydrodynamic drag on polymer molecules, is introduced (if $\alpha = 0$, the model reduces to the Oldroyd-B model). Numerical study showed that increasing α leads to a decrease in extensional viscosity and helps filaments neck down faster (Birjandi, Norouzi & Kayhani 2017). At sufficiently large values of α, the $1/3De$ exponential law breaks down at the beginning of uniaxial elongation of a filament, just when the continuously increasing elastic stress in the filament grows comparable to the characteristic capillary force σ/R (σ: surface tension coefficient; R: unperturbed thread radius); instead, the filament undergoes a much faster algebraic decrease in thickness (Ardekani *et al.* 2010). In the FENE model, the finite characteristic extensibility parameter L, which is the ratio of the length of a fully extended dumbbell to its equilibrium length, is introduced (if $L \to \infty$, the Oldroyd-B model is recovered) (Clasen *et al.* 2006*b*; Malkin *et al.* 2014; Mathues *et al.* 2018). Both numerical simulation and asymptotic analysis showed that in the later stages the minimum radius of a Giesekus or FENE polymer thread decreases linearly in time (Fontelos & Li 2004). Moreover, when inertia is non-negligible, the transition from a symmetric to an asymmetric profile occurs for filaments, that is, filaments lose their axial uniformity. In such a case, inertia plays a role in self-similarity of the neck region (Fontelos & Li 2004).

Two-phase flow systems in which a fluid jet or thread is immersed in a second fluid in a tube are ubiquitous in microfluidics, flow focusing, fuel atomization, emulsification and rheological applications (Lee 2003; Arratia *et al.* 2009; Zhao & Middelberg 2011; Du *et al.* 2016; Xie *et al.* 2019; Montanero & Gañán-Calvo 2020; Cabezas *et al.* 2021). An exterior fluid as well as the confinement of a tube may influence fundamentally jet configuration and resulting droplet size (Lister & Stone 1998; Montanero & Gañán-Calvo 2020). For the Newtonian case, a number of relevant studies have been reported (e.g. Tjahjadi, Stone & Ottino 1992; Sierou & Lister 2003; Homma *et al.* 2006; Wang 2013; Sousa *et al.* 2017). Particularly, Wang (2013) built a 1-D nonlinear model of a viscous fluid thread surrounded by a much less viscous fluid in a cylindrical tube and simulated numerically large deformations of the thread. The author found that increasing the tube radius results in a decrease in the breakup time of the thread and also an increase in the satellite drop size. Most interestingly, when the tube wall is placed close to the thread, the exterior fluid layer forces primary drops in the thread to form a 'plug with collar' structure, which is characterized by an abrupt rise of fluid interface in the neighbourhood of the pinch point.

Beyond Newtonian fluids, not many reports can be found in the literature. Among the few studies, Gunawan, Molenaar & wan de Ven (2005) investigated the linear instability of a viscoelastic fluid thread immersed in a Newtonian fluid inside a cylindrical tube, where fluid viscosities were considered to be high and the Reynolds numbers to be small.

Thus the equations governing the two-fluid system reduced to those for a creeping flow. On the other hand, the base flow (the steady axial velocities exhibit a parabolic profile under a constant pressure gradient) was taken into account. In the present work, a similar linear analysis is carried out, in which the problem is not limited to the creeping state but the base flow is neglected, in accordance with the conditions in our 1-D nonlinear model. Figueiredo *et al.* (2020) simulated numerically the 2-D axisymmetric stretch of an Oldroyd-B viscoelastic thread between two plates in the presence of an exterior Newtonian viscous fluid phase. In their simulation of the finitely long thread, the wavelength was fixed to three times the radius of the plates, which seems quite small compared to those in the case of infinitely long or semi-infinitely long threads or jets. It was found that the exterior Newtonian fluid does not prevent the formation of beads-on-a-string structures. However, the details of the structures may differ for different inner to outer fluid viscosity or density ratios.

To our knowledge, nonlinear dynamics of an infinitely long viscoelastic thread or jet in a confined geometry has not been reported yet. In this work we present a 1-D description of nonlinear behaviour of an Oldroyd-B or Giesekus viscoelastic thread surrounded by a Newtonian viscous fluid inside a cylindrical tube. The objective is to examine the effect of the surrounding fluid and the confinement on nonlinear evolution of the viscoelastic thread. The paper is organized as follows. In § 2, the theoretical model and the 1-D nonlinear equations describing the problem are presented. In § 3, a simple linear analysis is performed, the effect of the outer fluid and the confinement on the topological structure of the viscoelastic thread is explored and the nonlinear behaviour of Oldroyd-B and Giesekus viscoelastic threads is compared with each other. Finally, in § 4 the main conclusions are drawn.

2. One-dimensional model

Consider a two-fluid system confined in a cylindrical tube of radius R_0, as sketched in figure 1. Before being perturbed, the system is quiescent with no base flow; the interior fluid thread is an infinitely long cylinder of radius R. In this problem, our main concern is the effect of the surrounding immiscible fluid medium on the nonlinear deformation of the viscoelastic thread. For this purpose, the inner fluid is considered to be a polymer solution possessing viscoelasticity, and the outer fluid is Newtonian and viscous. The effect of the gravitational or buoyancy force, temperature and mass transfer is neglected. To facilitate the formulation, the cylindrical coordinate system (r, θ, z) with r, θ and z the radial, azimuthal and axial coordinates, respectively, is used to describe the problem. Upon a small-amplitude axisymmetric harmonic being imposed, the thread begins to deform, whose shape is a function of z and time t, denoted by $r = S(z, t)$.

Suppose that the viscoelasticity of the inner fluid is modelled by the Giesekus constitutive equation. The continuity equation, the momentum equation and the constitutive equations governing the inner fluid are

$$\nabla \cdot \boldsymbol{u}^i = 0, \tag{2.1}$$

$$\rho^i \left(\frac{\partial \boldsymbol{u}^i}{\partial t} + \boldsymbol{u}^i \cdot \nabla \boldsymbol{u}^i \right) = -\nabla p^i + \nabla \cdot \boldsymbol{T}_s^i + \nabla \cdot \boldsymbol{T}_p, \tag{2.2}$$

$$\boldsymbol{T}_s^i = 2\eta_s^i \boldsymbol{D}^i, \tag{2.3}$$

$$\boldsymbol{T}_p + \lambda^i \overset{\nabla}{\boldsymbol{T}}_p + \frac{\alpha \lambda^i}{\eta_p^i} (\boldsymbol{T}_p)^2 = 2\eta_p^i \boldsymbol{D}^i, \tag{2.4}$$

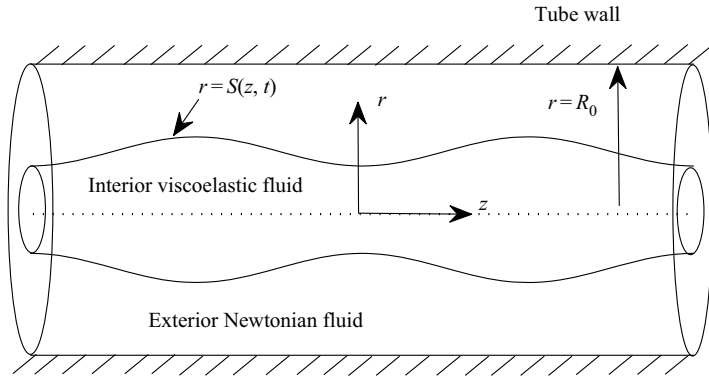*Dynamics of viscoelastic thread surrounded by Newtonian fluid*

Tube wall

Figure 1. Schematic illustration of an axisymmetric core–annular flow in a cylindrical tube.

where ρ is the density, p is the pressure, $\boldsymbol{u}$ is the velocity, η_s is the solvent viscosity, η_p is the polymer viscosity, $\boldsymbol{D}^i$ $(= \frac{1}{2}[\nabla \boldsymbol{u}^i + (\nabla \boldsymbol{u}^i)^{\mathrm{T}}]$ with T denoting the transpose) is the rate-of-strain tensor, $\boldsymbol{T}_s$ is the viscous stress from the solvent, $\boldsymbol{T}_p$ is the polymer stress, $\overset{\triangledown}{\boldsymbol{T}}_p$ is the upper-convected derivative of $\boldsymbol{T}_p$ defined by

$$\overset{\triangledown}{\boldsymbol{T}}_p = \frac{\partial \boldsymbol{T}_p}{\partial t} + \boldsymbol{u}^i \cdot \nabla \boldsymbol{T}_p - (\nabla \boldsymbol{u}^i)^{\mathrm{T}} \cdot \boldsymbol{T}_p - \boldsymbol{T}_p \cdot (\nabla \boldsymbol{u}^i)^{\mathrm{T}} \tag{2.5}$$

and the superscript i is used to denote the inner fluid.

For the outer Newtonian fluid, the governing equations are

$$\nabla \cdot \boldsymbol{u}^e = 0, \tag{2.6}$$

$$\rho^e \left(\frac{\partial \boldsymbol{u}^e}{\partial t} + \boldsymbol{u}^e \cdot \nabla \boldsymbol{u}^e \right) = -\nabla p^e + \nabla \cdot \boldsymbol{T}_s^e, \tag{2.7}$$

$$\boldsymbol{T}_s^e = 2\eta_s^e \boldsymbol{D}^e, \tag{2.8}$$

where η_s^e is the viscosity of the outer fluid and the superscript e is used to denote the outer fluid.

On the perturbed interface $r = S(z, t)$, the balance of the forces in the normal and tangential directions requires that

$$\boldsymbol{n} \cdot (-p^e \boldsymbol{I} + \boldsymbol{T}_s^e + p^i \boldsymbol{I} - \boldsymbol{T}_s^i - \boldsymbol{T}_p) \cdot \boldsymbol{n} = \sigma \kappa, \tag{2.9}$$

$$\boldsymbol{\tau} \cdot (-p^e \boldsymbol{I} + \boldsymbol{T}_s^e + p^i \boldsymbol{I} - \boldsymbol{T}_s^i - \boldsymbol{T}_p) \cdot \boldsymbol{n} = 0, \tag{2.10}$$

where $\boldsymbol{n}$ and $\boldsymbol{\tau}$ are the unit normal and tangential vectors on the interface given by

$$\boldsymbol{n} = \frac{1}{\sqrt{1 + \left(\dfrac{\partial S}{\partial z} \right)^2}} \left(-\frac{\partial S}{\partial z}, 1, 0 \right) \quad \text{and} \quad \boldsymbol{\tau} = \frac{1}{\sqrt{1 + \left(\dfrac{\partial S}{\partial z} \right)^2}} \left(1, \frac{\partial S}{\partial z}, 0 \right), \quad (2.11a,b)$$

respectively, and κ is the mean curvature given by

$$\kappa = \frac{1}{S \left[1 + \left(\dfrac{\partial S}{\partial z} \right)^2 \right]^{1/2}} - \frac{\dfrac{\partial^2 S}{\partial z^2}}{\left[1 + \left(\dfrac{\partial S}{\partial z} \right)^2 \right]^{3/2}}. \tag{2.12}$$

In addition, on the interface $r = S(z, t)$, the kinematic boundary condition and the continuity of velocity should be satisfied, i.e.

$$v^i = \frac{\partial S}{\partial t} + u^i \frac{\partial S}{\partial z}, \tag{2.13}$$

$$u^i = u^e, \quad v^i = v^e, \tag{2.14a,b}$$

where u and v are the axial and radial components of the velocity, respectively.

On the tube wall, the no-slip and no-penetration conditions are met, i.e.

$$u^e(R_0, z, t) = v^e(R_0, z, t) = 0. \tag{2.15}$$

If the radius of the thread varies gradually along the axial direction (the axial characteristic length l_z is much larger than the radial characteristic length l_r, i.e. $l_r/l_z \sim O(\varepsilon)$ with ε a small parameter), it can be considered as a slender body (Clasen *et al.* 2006a; Eggers & Villermaux 2008). On the other hand, in this two-fluid system, the outer fluid is assumed to be much lighter ($\rho^e/\rho^i \sim O(\varepsilon)$) and much less viscous ($\eta_0^e/\eta_0^i \sim O(\varepsilon^2)$) than the inner fluid. Although this restraint on the outer fluid greatly limits the generality of the two-fluid system, it allows us to derive a set of 1-D equations and helps get some insights into how the presence of an outer fluid affects the nonlinear evolution of a viscoelastic thread without too much computational cost. The same assumption was made in the 1-D study of two-fluid systems of viscous fluids in Lister & Stone (1998) and Wang (2013). The derivation of the 1-D equations and their dimensional form can be found in Appendix A. Choosing the unperturbed radius of the thread R, the capillary time $t_c = \sqrt{\rho^i R^3/\sigma}$, the zero-shear viscosity of the inner fluid $\eta_0^i = \eta_s^i + \eta_p^i$ and the capillary force σ/R as the scales of length, time, viscosity and pressure, respectively, the 1-D equations are non-dimensionalized as follows:

$$\frac{\partial(S^2)}{\partial t} + \frac{\partial(S^2 u^i)}{\partial z} = 0, \tag{2.16}$$

$$\frac{\partial u^i}{\partial t} + u^i \frac{\partial u^i}{\partial z} = \frac{3\beta Oh}{S^2} \frac{\partial\left(S^2 \frac{\partial u^i}{\partial z}\right)}{\partial z} + \frac{1}{S^2} \frac{\partial\left(S^2\left(\tau_{zz} - \tau_{rr}\right)\right)}{\partial z} - \frac{\partial \kappa}{\partial z} - \frac{2}{S^2} m_\eta Oh u^i G(S, d), \tag{2.17}$$

$$\tau_{zz} + De\left(\frac{\partial \tau_{zz}}{\partial t} + u^i \frac{\partial \tau_{zz}}{\partial z} - 2\tau_{zz} \frac{\partial u^i}{\partial z}\right) + \frac{\alpha De}{(1 - \beta)Oh} \tau_{zz}^2 = 2(1 - \beta)Oh \frac{\partial u^i}{\partial z}, \tag{2.18}$$

$$\tau_{rr} + De\left(\frac{\partial \tau_{rr}}{\partial t} + u^i \frac{\partial \tau_{rr}}{\partial z} + \tau_{rr} \frac{\partial u^i}{\partial z}\right) + \frac{\alpha De}{(1 - \beta)Oh} \tau_{rr}^2 = -(1 - \beta)Oh \frac{\partial u^i}{\partial z}, \tag{2.19}$$

where τ_{zz} and τ_{rr} are the zz and rr components of the tensor $\boldsymbol{T}_p$, respectively, $G(S, d) = (S^2 + d^2)/(S^2 - d^2 - (S^2 + d^2)\ln(S/d))$ and κ is the same in form as in (2.12). Note that the same symbols are used to denote both the dimensional and corresponding non-dimensional quantities. The non-dimensional parameters involved in the 1-D equations are: the Ohnesorge number $Oh = \eta_0^i/\sqrt{\rho^i \sigma R}$ representing the relative importance of viscosity and capillarity, the Deborah number $De = \lambda^i/t_c$ measuring the relative importance of elasticity and capillarity, the solvent to solution viscosity ratio of the inner fluid $\beta = \eta_s^i/\eta_0^i$, the outer to inner fluid viscosity ratio $m_\eta = \eta_0^e/\eta_0^i$, the mobility factor α and the tube to thread radius ratio $d = R_0/R$. When the viscosity ratio m_η is

equal to zero, the 1-D model is reduced to that for a single Giesekus viscoelastic thread in vacuum (Fontelos & Li 2004; Ardekani *et al.* 2010). If the mobility factor α is set to zero, the 1-D model represents that for an Oldroyd-B viscoelastic thread surrounded by a Newtonian fluid inside a tube.

3. Numerical results

The 1-D equations (2.16)–(2.19) are solved using an implicit finite difference scheme (first-order backward method in time, upwind scheme for the convective terms and central difference method for the dissipation terms), where the Newton–Raphson technique is used to solve the nonlinear algebraic equations at each time step. To better simulate large deformations at large times, non-uniform grids with an adaptive grid refinement are used in the spatial discretization. Considering both accuracy and efficiency, the number of discrete points is usually between 1000 and 1400, and the time step varies between 10^{-6} and 0.001. At each time step, it requires that the maximum relative errors of all quantities are less than 0.1 %. The calculation is terminated when the minimum radius of the thread is below 0.001. The validity of the code is checked by comparing with the results in Clasen *et al.* (2006*a*) and Ardekani *et al.* (2010).

At the initial time, the thread is assumed to be perturbed by a small cosinoidal harmonic, i.e.

$$S(z, t = 0) = \sqrt{1 - \epsilon_0^2/2} + \epsilon_0 \cos(kz), \tag{3.1}$$

where $k = 2\pi/\lambda$ is the axial wavenumber and ϵ_0 is the initial amplitude of the disturbance whose value is fixed to 0.01.

Considering the spatial periodicity and symmetry of the system, only a half-wavelength-long segment $z \in [0, \lambda/2]$ is calculated, where λ is the wavelength. The periodic boundary conditions are imposed at two ends of the segment, i.e.

$$\left.\begin{aligned}
\frac{\partial S}{\partial z}(z = 0, t) = \frac{\partial S}{\partial z}\left(z = \frac{\lambda}{2}, t\right) = 0, \quad u^i(z = 0, t) = u^i\left(z = \frac{\lambda}{2}, t\right) = 0, \\
\frac{\partial \tau_{zz}}{\partial z}(z = 0, t) = \frac{\partial \tau_{zz}}{\partial z}\left(z = \frac{\lambda}{2}, t\right) = 0, \quad \frac{\partial \tau_{rr}}{\partial z}(z = 0, t) = \frac{\partial \tau_{rr}}{\partial z}\left(z = \frac{\lambda}{2}, t\right) = 0.
\end{aligned}\right\} \tag{3.2}$$

Suppose that the density of the polymer solution $\rho^i = 1000$ kg m^{-3}, the zero-shear viscosity $\eta_0^i = 0.1$ Pa s, the stress relaxation time $\lambda^i = 0.5$ ms and the interface tension coefficient $\sigma = 0.05$ N m^{-1}. Such a fluid is of high viscoelasticity. The radius of the thread is supposed to be 100 μm. Thus the Ohnesorge number $Oh = 1.4$ and the Deborah number $De = 3.5$, the values of which are quite close to the estimation in Ardekani *et al.* (2010). Without loss of generality, the viscosity ratio β is fixed to 0.5. The viscosity ratio m_η must be small, which ranges from 0 to 0.04 in the calculation. The mobility factor α is also maintained to be small, varying between 0 and 0.005. The axial wavenumber k must be within the instability region, and we take $k \in [0.3, 0.9]$ in the calculation. As for the radius ratio d, its value must be large enough to prevent the inner fluid thread from touching the tube wall at large deformations. In the computation, the constraint $d \geq 2$ may ensure the avoidance of touchdown phenomenon.

3.1. *Linear instability analysis*

The behaviour of the perturbed viscoelastic thread at small times and the effect of the relevant parameters on it can be predicted by linear theory. In this subsection a simple linear instability analysis is performed. Linearizing the 1-D equations (2.16)–(2.19) and substituting the following normal mode decompositions into them:

$$S = 1 + \hat{S} \exp(\omega t + jkz) + \text{c.c.}, \tag{3.3}$$

$$u^i = \hat{u}^i \exp(\omega t + jkz) + \text{c.c.}, \tag{3.4}$$

$$\tau_{zz} = \hat{\tau}_{zz} \exp(\omega t + jkz) + \text{c.c.}, \tag{3.5}$$

$$\tau_{rr} = \hat{\tau}_{rr} \exp(\omega t + jkz) + \text{c.c.}, \tag{3.6}$$

where the hat denotes the initial amplitudes of the perturbations, ω is the complex frequency (with real part ω_r the temporal growth rate and imaginary part ω_i the speed of wave propagation), 'c.c.' denotes the complex conjugate and j is the imaginary unit, one obtains the following dispersion relation:

$$\omega \left(\omega + 3\beta Ohk^2 + \frac{3(1-\beta)Ohk^2}{1 + De\omega} \right) - \frac{k^2(1-k^2)}{2} + 2\omega m_\eta OhG(1, d) = 0. \tag{3.7}$$

Note that the mobility factor α for Giesekus fluids does not appear in (3.7). When $De = 0$, (3.7) reduces to that for the Newtonian viscous case (Wang 2013); let m_η be 0, and (3.7) reduces to that for an Oldroyd-B or Giesekus viscoelastic thread in vacuum.

The dispersion relation for the 2-D axisymmetric instability of the thread is also derived. The derivation process is straightforward. Some details can be found in Appendix B. Finally, the dispersion relation is written as

$$\begin{vmatrix} a_{11} & a_{12} & a_{13} & a_{14} & a_{15} & a_{16} \\ a_{21} & a_{22} & a_{23} & a_{24} & a_{25} & a_{26} \\ I_1(k) & I_1(k^i) & -I_1(k) & -K_1(k) & -I_1(k^e) & -K_1(k^e) \\ kI_0(k) & k^i I_0(k^i) & -kI_0(k) & kK_0(k) & -k^e I_0(k^e) & k^e K_0(k^e) \\ 0 & 0 & I_1(kd) & K_1(kd) & I_1(k^e d) & K_1(k^e d) \\ 0 & 0 & -kI_0(kd) & kK_0(kd) & -k^e I_0(k^e d) & k^e K_0(k^e d) \end{vmatrix} = 0, \tag{3.8}$$

where

$$a_{11} = \frac{\omega I_0(k)}{Oh} + 2k^2 I_1'(k)\frac{1 + \beta\omega De}{1 + \omega De} + \frac{1}{\omega Oh}k(k^2 - 1)I_1(k),$$

$$a_{12} = 2kk^i I_1'(k^i)\frac{1 + \beta\omega De}{1 + \omega De} + \frac{k(k^2 - 1)}{\omega Oh}I_1(k^i),$$

$$a_{13} = -\frac{m_\rho \omega}{Oh}I_0(k) - 2m_\eta k^2 I_1'(k), \quad a_{14} = m_\rho \frac{\omega}{Oh}K_0(k) - 2m_\eta k^2 K_1'(k),$$

$$a_{15} = -2m_\eta kk^e I_1'(k^e), \quad a_{16} = -2m_\eta kk^e K_1'(k^e),$$

$$a_{21} = -2k^2 I_1(k)\frac{1 + \beta\omega De}{1 + \omega De}, \quad a_{22} = -(k^2 + (k^i)^2)I_1(k^i)\frac{1 + \beta\omega De}{1 + \omega De}, \quad a_{23} = 2m_\eta k^2 I_1(k),$$

$$a_{24} = 2m_\eta k^2 K_1(k), \quad a_{25} = m_\eta(k^2 + (k^e)^2)I_1(k^e),$$
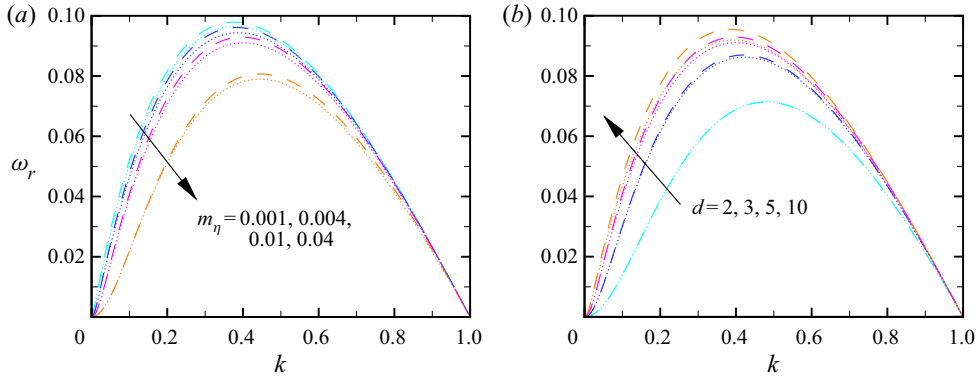
$$a_{26} = m_\eta(k^2 + (k^e)^2)K_1(k^e), \tag{3.9}$$

Figure 2. The temporal growth rate ω_r versus the axial wavenumber k. (a) The effect of the outer to inner fluid viscosity ratio m_η, where $d = 5$, and (b) the effect of the tube to thread radius ratio d, where $m_\eta = 0.01$. Dashed: the slender body approximation; dotted: the 2-D linear instability analysis. The arrows denote the direction of a parameter increasing. Here $Oh = 1.4$, $\beta = 0.5$, $De = 3.5$, $m_\rho = 0.1$.

$I_n(\cdot)$ and $K_n(\cdot)$ ($n = 0, 1$) are the nth-order modified Bessel functions of the first and second kinds, respectively, $k^i = \sqrt{k^2 + \omega(1 + \omega De)/Oh(1 + \beta\omega De)}$, $k^e = \sqrt{k^2 + m_\rho\omega/m_\eta Oh}$ and $m_\rho = \rho^e/\rho^i$ is defined as the outer to inner fluid density ratio. Note that the mobility factor α of the Giesekus model, which turns out to be a secondary factor in linear analysis, is absent from (3.8).

The effect of the viscosity ratio m_η and the radius ratio d on the temporal growth rate ω_r is shown in figures 2(a) and 2(b), respectively. Clearly, as m_η increases or d decreases, ω_r decreases. This indicates that both the outer viscous fluid layer and the confinement of the tube suppress the instability of the viscoelastic thread. It is also found that when d exceeds 10, ω_r is little changed on increasing d further, as reported by Gunawan *et al.* (2005). Note that the cut-off wavenumber beyond which the thread is stable is maintained at unity, regardless of the value of m_η or d. A comparison of the 1-D and 2-D results shows that the slender body approximation overestimates the growth rate at moderate wavenumbers but it predicts well the linear instability of the thread at small wavenumbers, as reported by Wang (2013) in a study of Newtonian threads.

3.2. *Nonlinear behaviour of an Oldroyd-B viscoelastic thread surrounded by a viscous fluid in a tube*

In this subsection the mobility factor α is fixed to zero and we study the effect of the surrounding viscous fluid layer and the confinement of the tube on the nonlinear behaviour of the Oldroyd-B viscoelastic thread. As is well known, a single Oldroyd-B viscoelastic thread in vacuum evolves into a beads-on-a-string structure with or without secondary droplets; if there is no secondary droplet, the stretched filament between primary droplets necks down following the $1/3De$ exponential law in time (Chang *et al.* 1999; Clasen *et al.* 2006a; Ardekani *et al.* 2010). Here we show that the presence of an outer fluid phase may influence substantially the topological structures of Oldroyd-B viscoelastic threads.

Typical thread profiles are illustrated in figure 3, where the axial wavenumber k is fixed to 0.9. As shown in figure 3(a), for such a large wavenumber, no satellite droplet is formed in an Oldroyd-B viscoelastic thread in vacuum ($m_\eta = 0$). When m_η is increased to a small value, 0.001 in figure 3(b), a very small secondary droplet appears at the midpoint of the
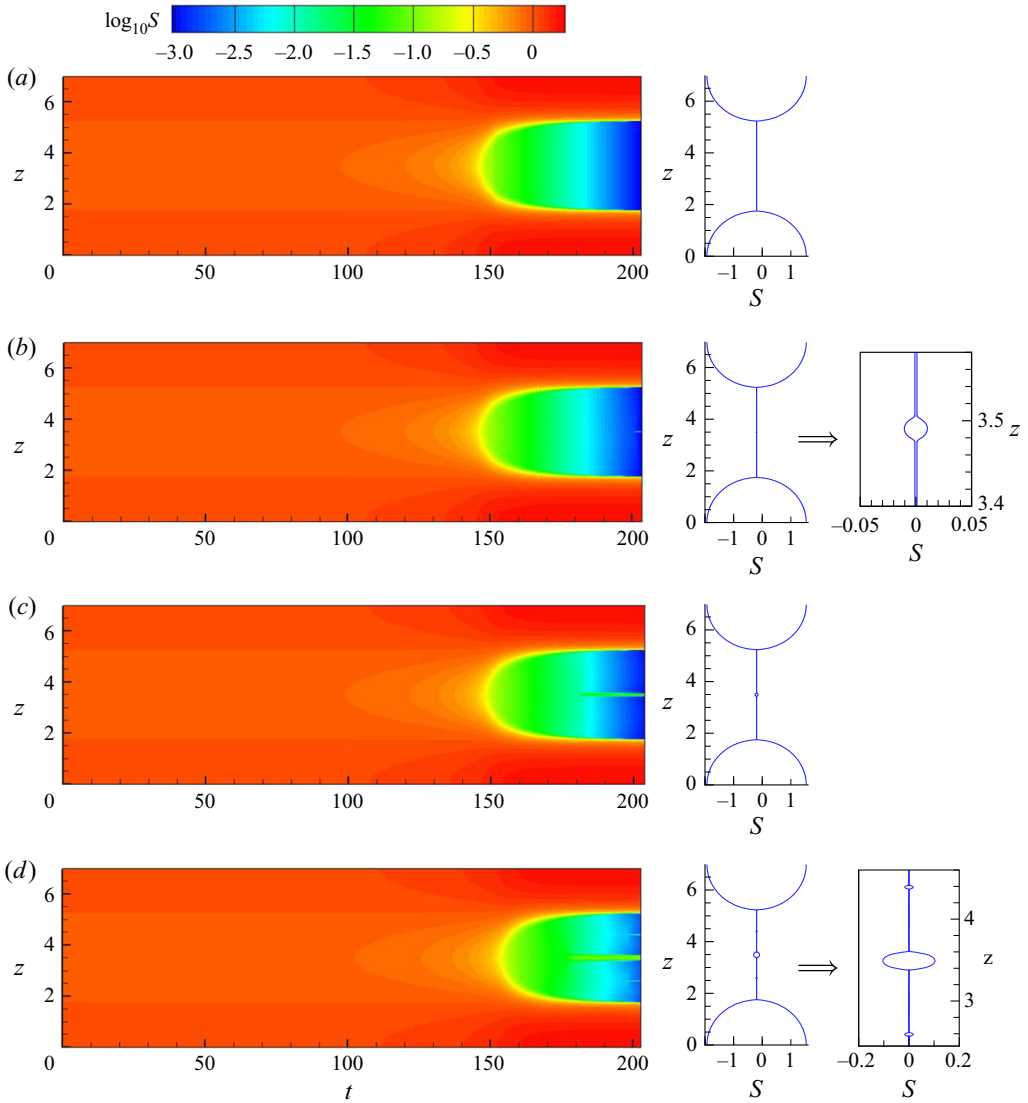
Figure 3. Space–time diagrams of the evolution of the Oldroyd-B viscoelastic thread and its profile. The viscosity ratio (*a*) $m_\eta = 0$, (*b*) $m_\eta = 0.001$, (*c*) $m_\eta = 0.01$ and (*d*) $m_\eta = 0.04$. Here $k = 0.9, Oh = 1.4, \beta = 0.5, De = 3.5, d = 5, \alpha = 0$.

filament; see the zoomed-in plot on the right-hand side for clarity. Due to the formation of this secondary droplet, the axial uniformity of the entire filament collapses and the extensional flow in it is rearranged. As m_η is further increased, the size of the secondary droplet at the midpoint is continuously increased, as shown in figure 3(*c*,*d*). When m_η is large enough, in addition to the droplet at the midpoint, even smaller secondary droplets appear in the filament (see figure 3*d*). Generally, the presence of the outer viscous fluid phase gives rise to the formation of secondary droplets. Moreover, the space–time diagrams demonstrate that secondary droplets start to form at earlier times for larger viscosities of the outer fluid.
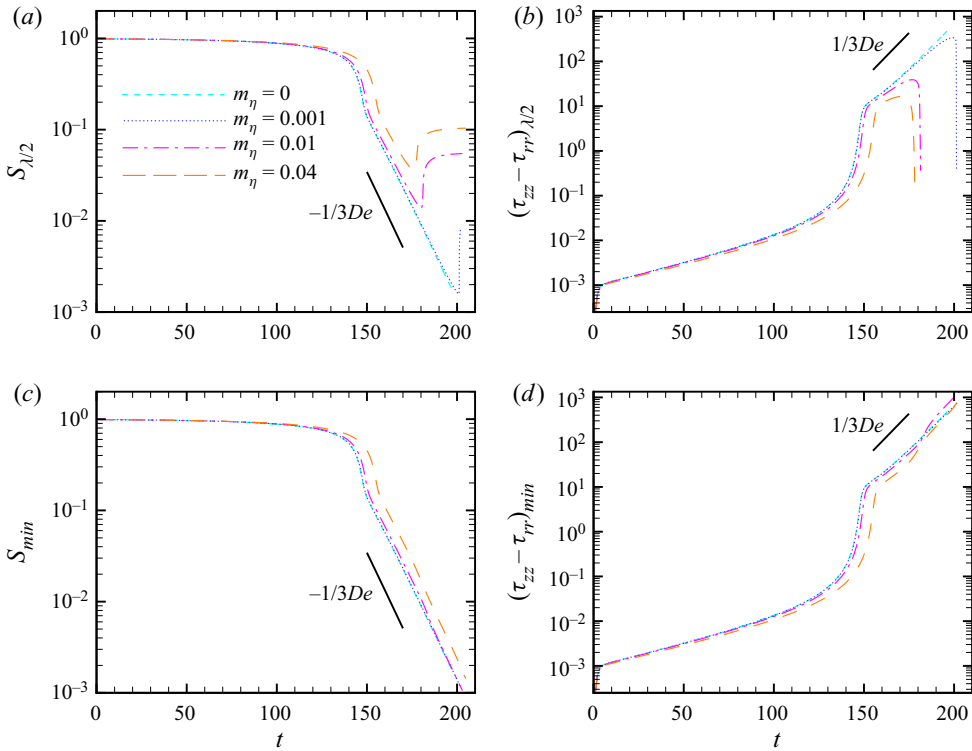
Figure 4. Effect of the viscosity ratio m_η on the evolution of the Oldroyd-B viscoelastic thread. (*a*) The thread radius S at the midpoint $z = \lambda/2$, (*b*) the first normal stress difference $\tau_{zz} - \tau_{rr}$ at $z = \lambda/2$, (*c*) the minimum thread radius S_{min} and (*d*) $\tau_{zz} - \tau_{rr}$ at S_{min}. Here $k = 0.9$, $Oh = 1.4$, $\beta = 0.5$, $De = 3.5$, $d = 5$, $\alpha = 0$.

The space–time diagrams in figure 3 also demonstrate the suppression effect of the outer viscous phase on the instability of the thread. As m_η continuously increases, the thread thickness at the midpoint $z = \lambda/2$, where the trough of the initial harmonic perturbation is located, decreases more and more slowly. This trend is clearly shown in figure 4, where the variation of both the thread radius S and the first normal stress difference $\tau_{zz} - \tau_{rr}$ with time is illustrated. Note that due to the small growth rate of the wavenumber $k = 0.9$ as predicted by linear theory (see figure 2), the perturbation on the thread grows very slowly in the linear stage. Moreover, as m_η increases, the decrease in the thread radius gets slower. Beyond the linear range, as shown in figure 4(*a*), the thread radius at the midpoint, $S_{\lambda/2}$, undergoes first a fast decrease dominated by the inertial and capillary forces, and then steps into a relatively slow decrease stage in which the elastic and capillary forces presumably play a role (Clasen *et al.* 2006*a*). In the elasto-capillary regime, if the outer fluid phase exists, the decrease in $S_{\lambda/2}$ does not follow the $1/3De$ exponential law as in vacuum, which appears to be slightly slower. Most significantly, at some instant, $S_{\lambda/2}$ starts to increase, indicating that a secondary droplet is being formed at the midpoint. With the formation of the secondary droplet, the polymeric stress at the midpoint decreases rapidly, as shown in figure 4(*b*). Ultimately the first normal stress difference $\tau_{zz} - \tau_{rr}$ approaches zero and ends up with a small negative value, which is not illustrated in the semi-logarithmic plot in figure 4(*b*).

The variation of the minimum thread radius S_{min} with time is shown in figure 4(*c*). Surprisingly, while the secondary droplet at the midpoint is formed, the decrease of S_{min}
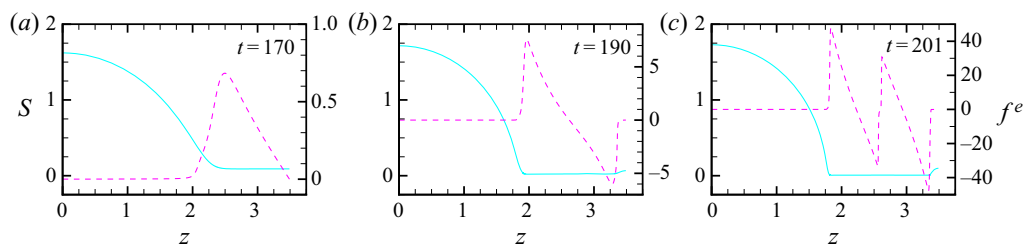
Figure 5. The thread profile S (solid lines) and the force exerted on the thread by the outer fluid f^e (dashed lines) at different instants. Here $k = 0.9$, $Oh = 1.4$, $\beta = 0.5$, $De = 3.5$, $m_\eta = 0.01$, $d = 5$, $\alpha = 0$.

gets slightly faster, with a rate slightly (about 2 %) higher than $1/3De$. The polymeric stress at S_{min} experiences an increase greater than the $1/3De$ law at the moment the secondary droplet begins to form, as shown in figure 4(*d*). After the secondary droplet is formed, the distribution of the forces along the filament, especially the capillary and elastic forces, is substantially changed.

To better understand the effect of the outer viscous fluid phase on the stretch of the thread, the force exerted on the thread by the outer fluid, expressed as $f^e = -2m_\eta Oh u^i G(s, d)/S^2$ in the 1-D momentum equation (2.17), is calculated and diagrammed in figure 5 for $k = 0.9$, $m_\eta = 0.04$ and three time instants $t = 170$, 190 and 201, where a half-wavelength-long segment of the thread $z \in [0, \lambda/2]$ is plotted. At $t = 170$, the secondary droplet at the midpoint has not been formed yet, and the thickness of the stretched filament between primary droplets is almost axially uniform. The force exerted by the outer fluid, f^e, is positive in the entire filament (see figure 5*a*), indicating that the outer fluid tends to stop fluid particles in the filament from moving towards the primary droplet and slows down the thinning of the filament, as shown in figure 4(*a*). That is, f^e acts as a resistance to the extensional flow in the filament. This force induces the non-uniformity of the filament thickness gradually. In figure 5(*b*), at $t = 190$, the non-uniformity becomes more evident, with a mild hump appearing at the midpoint. In the neighbourhood of the midpoint the elastic stress decreases dramatically to almost zero. Under the action of the capillary pressure, the small hump eventually obtains a spheroidal shape, as shown in figure 5(*c*). On the other hand, from the distribution of f^e in the filament between the primary droplet and the hump in figure 5(*b*), the outer fluid still resists the thinning of the filament. At $t = 201$, the double-fold configuration of f^e indicates that another secondary droplet is going to be formed at some location. Indeed, for $m_\eta = 0.04$, two generations of secondary droplets exist in the filament, as shown in figure 3(*d*). As the filament is stretched, f^e is increased, but it remains as a secondary factor compared with the capillary and elastic forces. So its resisting effect on the filament thinning is quite limited all the time, as illustrated in figure 4(*c*).

At smaller wavenumbers, the scenario is similar. That is, the outer viscous fluid tends to induce the formation of secondary droplets on the filament. As shown in figure 6 where the axial wavenumber $k = 0.3$, when the viscosity ratio m_η is increased from 0 to 0.01, more generations of secondary droplets are produced successively. Different generations have difference sizes, and those smallest secondary droplets are hardly seen in the figure. This beads-on-a-string structure with multiple secondary droplets, described by Kamat *et al.* (2018) as micro-thread cascades, may also be induced by a surfactant or an imposed electric field (Li, Yin & Yin 2017*b*; Kamat *et al.* 2018; Li *et al.* 2019). The space–time
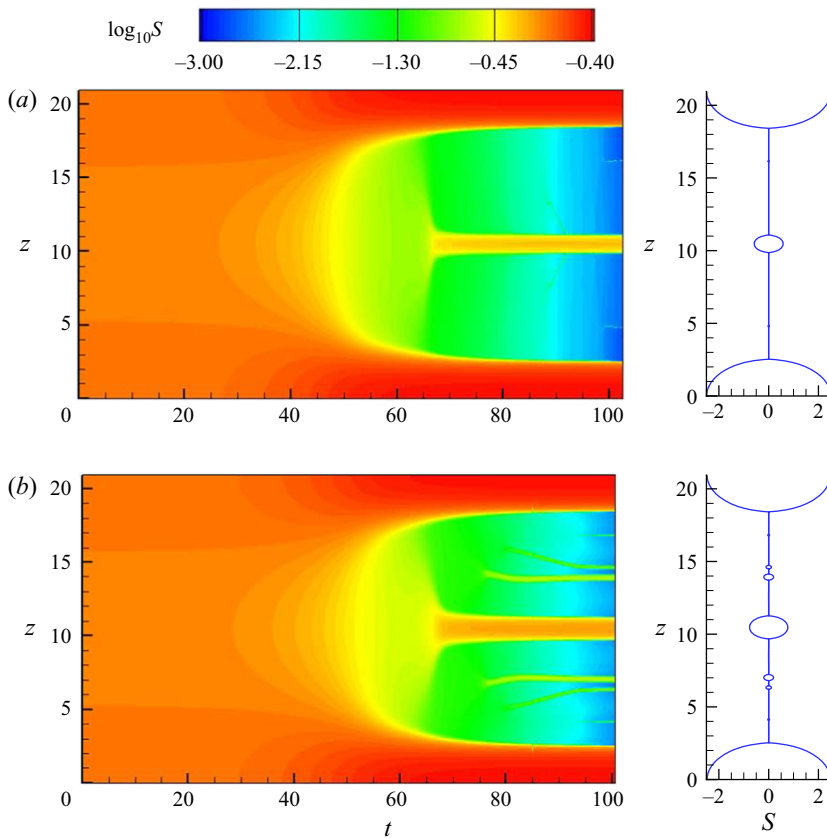
926 A21-12

Figure 6. Space–time diagrams of the evolution of the Oldroyd-B viscoelastic thread and its profile for (a) $m_\eta = 0$ and (b) $m_\eta = 0.01$. Here $k = 0.3$, $Oh = 1.4$, $\beta = 0.5$, $De = 3.5$, $d = 5$, $\alpha = 0$.

diagrams demonstrate that the necking of the thread is slowed down to a certain extent by the outer fluid phase.

The axial wavenumber k is considered to be an important parameter influencing the topological structure of a viscoelastic thread (Ardekani *et al.* 2010). We diagram the situation in the (k, m_η) plane in figure 7, where for each couple of k and m_η the number of secondary droplets is counted. Generally, as k decreases or m_η increases, more secondary droplets appear in the filament between two adjacent primary droplets. Even when the viscosity of the outer fluid is very small (the smallest value of m_η in the calculation is 0.001), at least one secondary droplet is formed, regardless of the value of the axial wavenumber. It seems that the appearance of secondary droplets is unavoidable in the presence of an outer viscous fluid. Differently, in the absence of an outer fluid phase, at large wavenumbers, such as $k = 0.8$ or 0.9 as shown in figure 7, there is no satellite droplet formed in beads-on-a-string structure (Ardekani *et al.* 2010; Keshavarz *et al.* 2015). Our simulation result shows that the presence of an outer fluid phase does not favour the formation of a uniform filament that is expected in applications such as fluid bridge and extensional rheometer (Ardekani *et al.* 2010; Mathues *et al.* 2018; Figueiredo *et al.* 2020).

The effect of the confinement on the Oldroyd-B viscoelastic thread is examined in figure 8, where the radius ratio d varies from 2 to 10. In figures 8(*a*) and 8(*b*), two-wavelength-long thread segments are plotted for $k = 0.3$ and $k = 0.9$, respectively.
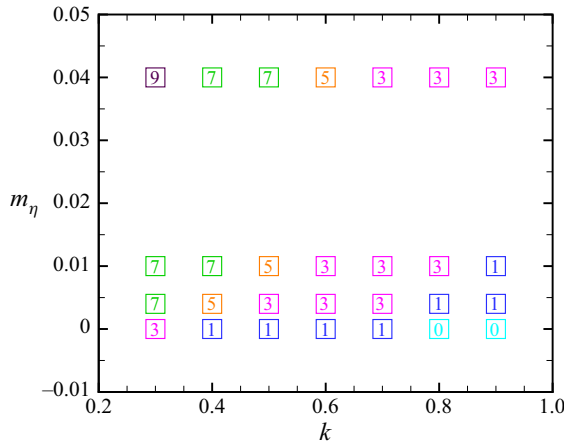
926 A21-13

Figure 7. The statistics of secondary droplets in the (k, m_η) plane. The numbers indicate how many secondary droplets are formed in the filament between two adjacent primary droplets. Here $Oh = 1.4$, $\beta = 0.5$, $De = 3.5$, $d = 5$, $\alpha = 0$.

It is shown that for all values of d considered, the thread evolves into a quite similar beads-on-a-string structure. Not like the viscosity ratio m_η, the confinement hardly influences the topological structure of a fully stretched thread. In addition, a closer observation finds that as d decreases the sizes of secondary droplets of all generations are increased slightly; see the zoomed-in plots in figures 8(a) and 8(b). That is, the confinement helps secondary droplets gain some weight.

Figure 8(c) shows the time evolution of the minimum thread radius S_{min} for $k = 0.9$, where the location of S_{min}, i.e. z_{min} (relative to half-wavelength $\lambda/2$), is plotted as well. As d decreases, the decrease of S_{min} is slowed down, indicating that the confinement has a stabilization effect on the perturbed thread, which is well predicted by linear theory in figure 2(b). Initially, S_{min} is located at the midpoint of the thread, $z_{min}/(\lambda/2)$ being equal to 1. Later, when the deformation of the thread enters the elasto-capillary stage, z_{min} moves away from the midpoint $z = \lambda/2$. Ultimately, S_{min} is located in the neck region joining the filament to the primary droplet where $z_{min}/(\lambda/2) \simeq 0.5$. Generally, for different values of d, the variation of S_{min} with time is quite similar in the elasto-capillary stage. The time evolution of the first normal stress difference $\tau_{zz} - \tau_{rr}$ at S_{min} is also similar for all values of d, as shown in figure 8(d).

Given the thread profile S and the axial velocity u, the force exerted by the outer fluid phase, f^e, is calculated for different values of the radius ratio d. The relevant results are shown in figure 9, where two typical time instants are plotted. At $t = 179$, the thread exhibits a beads-on-a-string profile in which the secondary droplet is not formed yet (see figure 9a). The filament between primary droplets is almost axially uniform. The force exerted by the outer fluid, f^e, is positive in the filament (see figure 9c), which serves as a resistance to the extensional flow. As d decreases, f^e increases, indicating that the confinement enhances the influence of the outer fluid phase on the deformation of the thread. From the distribution of the axial velocity in the filament shown in figure 9(a), the extension rate $\partial u/\partial z$ deviates from $2/3De$ of an Oldroyd-B viscoelastic thread in vacuum. This is understandable, considering that f^e is a resistance which decelerates the motion of fluid particles in the filament. Basically, away from the midpoint of the filament, the extension rate becomes larger. The extensional flow with a spatially varying extension rate implies that the filament thickness can no longer be uniform. Close to the primary
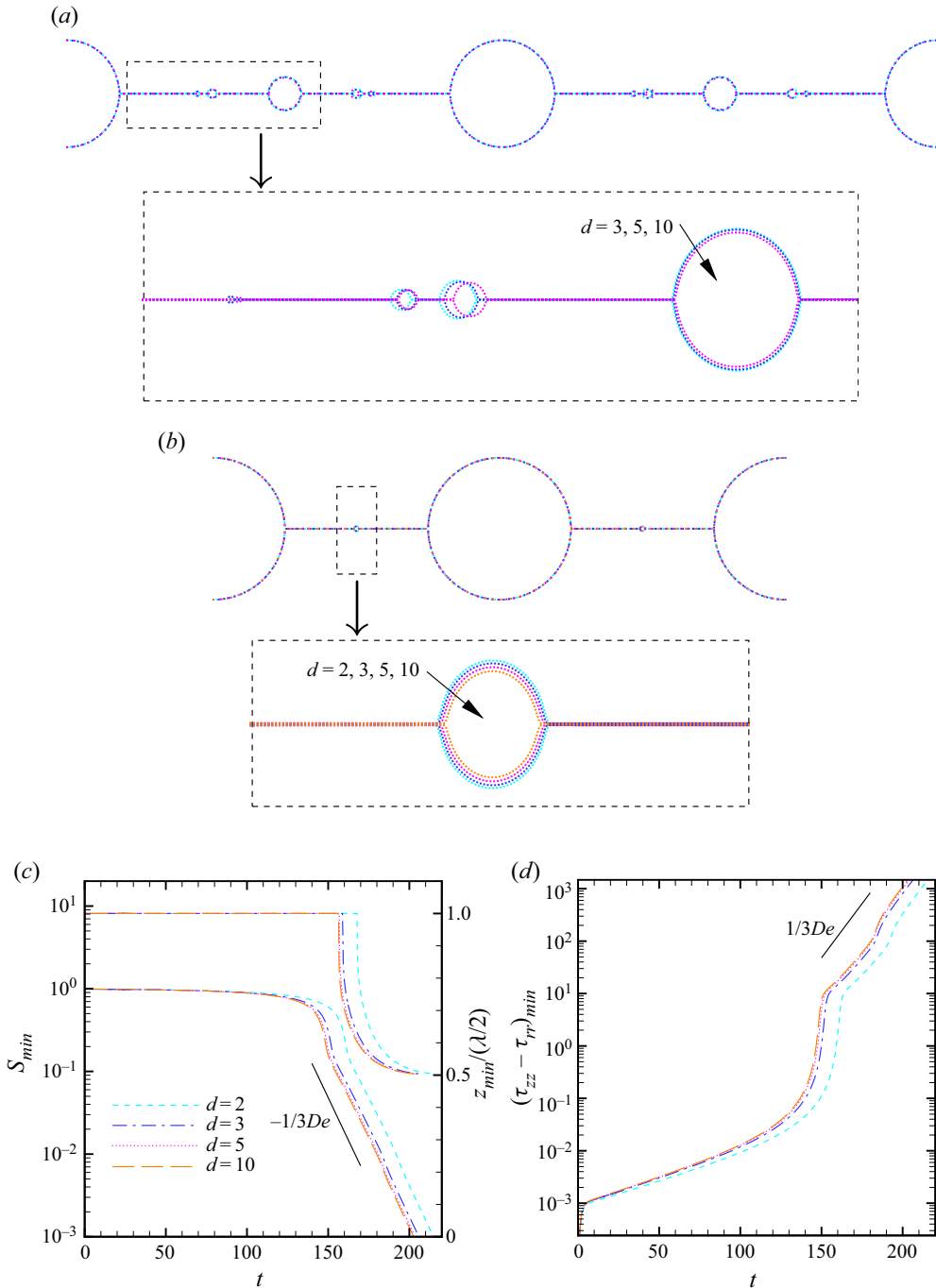
926 A21-14

Figure 8. Effect of the radius ratio d on the nonlinear behaviour of the Oldroyd-B viscoelastic thread. The thread profile for (*a*) $k = 0.3$ and (*b*) $k = 0.9$ as d varies. The arrows denote the direction of d increasing. The variation of (*c*) the minimum thread radius S_{min} (the lower lines) and the corresponding location z_{min} (the upper lines) and (*d*) the first normal stress difference $\tau_{zz} - \tau_{rr}$ at S_{min} with time, where $k = 0.9$. Here $Oh = 1.4, \beta = 0.5, De = 3.5, m_\eta = 0.01, \alpha = 0$.
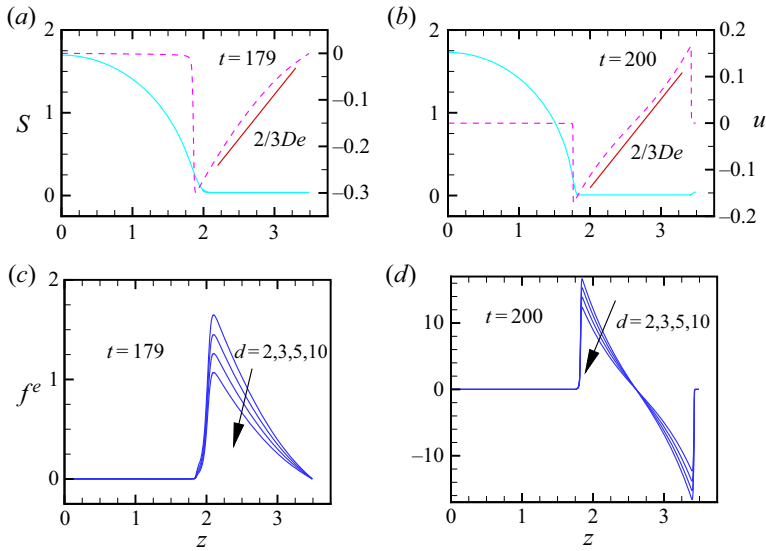
Figure 9. (*a,b*) The thread profile S (solid lines) and the axial velocity u (dashed lines) and (*c,d*) the force exerted on the thread by the outer fluid f^e at two typical instants. The arrows denote the direction of d increasing. Here $k = 0.9$, $Oh = 1.4$, $\beta = 0.5$, $De = 3.5$, $m_\eta = 0.01$, $\alpha = 0$.

droplet, the filament is more stretched. At the later time $t = 200$, the secondary droplet at the midpoint is about to be shaped (see figure 9*b*). The distribution of the force in figure 9(*d*) suggests that f^e is still a resistance. As d decreases, f^e increases, resulting in a larger size of secondary droplet, as shown in figure 8. In figure 9(*b*), the axial velocity in the filament deviates slightly from the $2/3De$ slope, and the trend that the extension rate varies along the axial direction suggests that the filament is most stretched in the neck regions.

3.3. *Nonlinear behaviour of a Giesekus viscoelastic thread surrounded by a viscous fluid in a tube*

For a Giesekus viscoelastic thread, breakup occurs in a finite time. It is well established that at the final stages prior to pinch-off, the minimum radius of a Giesekus viscoelastic thread approaches zero linearly with time, i.e. $S_{min} \sim (t_p - t)$, where t_p is the pinching time (Fontelos & Li 2004; Ardekani *et al.* 2010). In this study, it is found that an outer viscous fluid affects the topological structure of a Giesekus thread in a way similar to how it affects an Oldroyd-B thread. Some results are shown in figure 10.

In figure 10, four different cases, i.e. an Oldroyd-B thread in vacuum ($m_\eta = 0, \alpha = 0$), an Oldroyd-B thread surrounded by a viscous fluid ($m_\eta = 0.01, \alpha = 0$), a Giesekus thread in vacuum ($m_\eta = 0, \alpha = 0.005$) and a Giesekus thread surrounded by a viscous fluid ($m_\eta = 0.01, \alpha = 0.005$), are presented for comparison. For the relatively large axial wavenumber $k = 0.8$ considered in the figure, in the absence of the outer fluid phase, no secondary droplet is formed at the midpoint of the filament, regardless of fluid type; in the presence of an outer fluid, secondary droplets always appear in the thread, although the sizes of them are different for Oldroyd-B and Giesekus fluids, as can be seen from the thread profiles in figure 10(*a*). As shown in figure 10(*b*), the Oldroyd-B thread in vacuum necks down following the $1/3De$ exponential law in the elasto-capillary stage. Differently, the thickness of the Giesekus thread in vacuum decreases much more rapidly
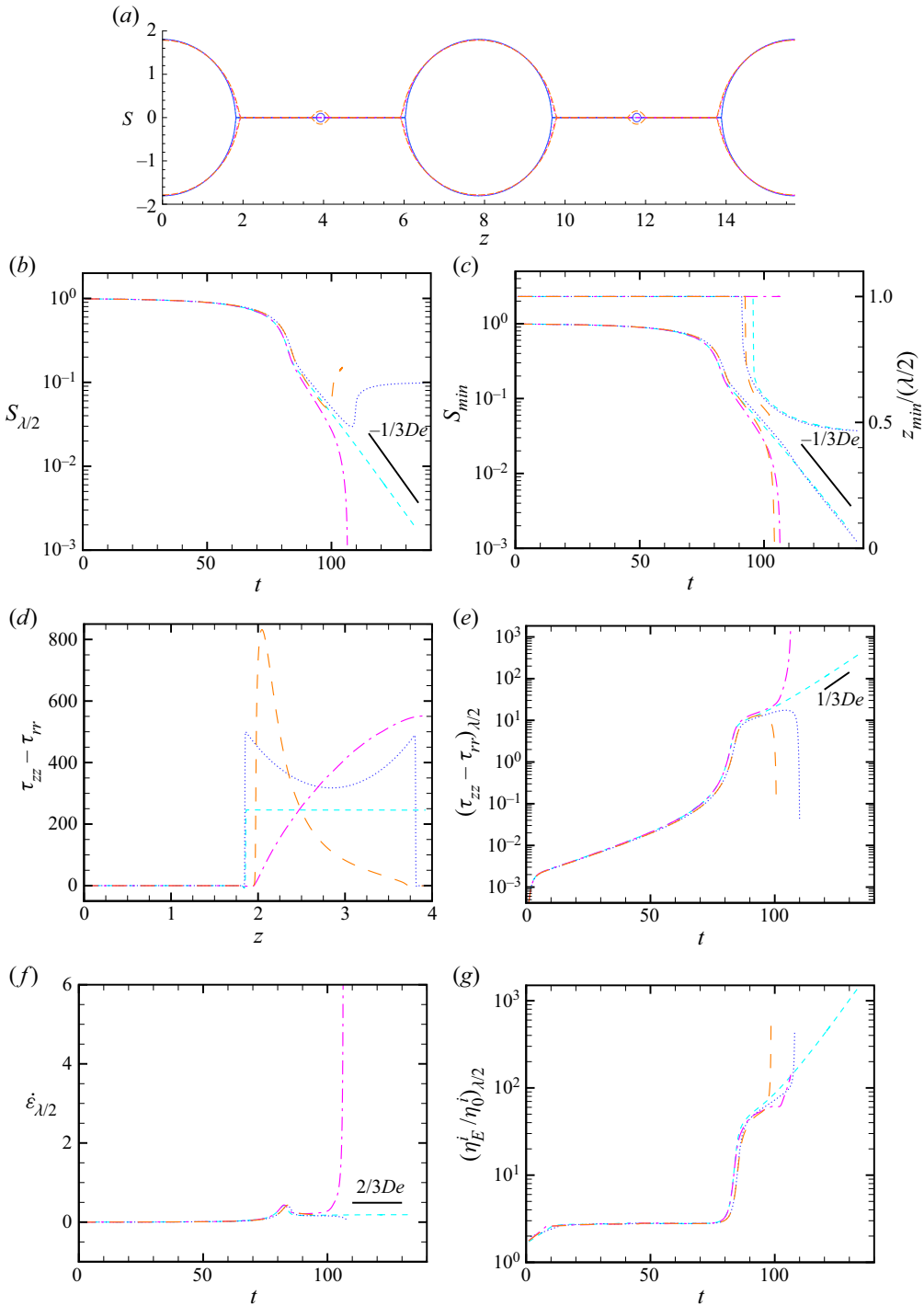
Figure 10. Comparison of Oldroyd-B and Giesekus viscoelastic fluid threads in vacuum or surrounded by an outer viscous fluid. (*a*) The thread profile. (*b*) The time evolution of the thread radius S at the midpoint $z = \lambda/2$. (*c*) The minimum thread radius S_{min} (the lower lines) and its location $z_{min}/(\lambda/2)$ (the upper lines). (*d*) Typical distribution of $\tau_{zz} - \tau_{rr}$ along the thread, where $z \in [0, \lambda/2]$. (*e*) The first normal stress difference $\tau_{zz} - \tau_{rr}$ at $z = \lambda/2$. (*f*) The extension rate $\dot{\varepsilon}$ at $z = \lambda/2$. (*g*) The Trouton ratio η_E^i/η_0^i at $z = \lambda/2$. Short dashed: $m_\eta = 0, \alpha = 0$; dotted: $m_\eta = 0.01, \alpha = 0$; dash-dotted: $m_\eta = 0, \alpha = 0.005$; long dashed: $m_\eta = 0.01, \alpha = 0.005$. Here $k = 0.8, Oh = 1.4, \beta = 0.5, De = 3.5, d = 5$.

and reaches zero at t_p. In the presence of the outer viscous fluid phase, $S_{\lambda/2}$ of either Oldroyd-B or Giesekus thread starts to increase at some instant, indicating the formation of a secondary droplet at the midpoint. Moreover, the final $S_{\lambda/2}$ for the Giesekus thread is larger, indicating that its secondary droplet is larger. Fontelos & Li (2004) found that due to the non-zero mobility factor α, a Giesekus viscoelastic filament in vacuum may lose its uniformity. In this problem, apart from the mobility factor, the outer fluid phase is also a factor inducing the non-uniformity of the filament. Accompanied by the formation of the secondary droplet, the decrease in the minimum thread radius of both Oldroyd-B and Giesekus threads becomes a little faster than in the case of no outer fluid, as illustrated in figure 10(*c*).

Typical distribution of the first normal stress difference $\tau_{zz} - \tau_{rr}$ at large times is presented in figure 10(*d*) for a half-wavelength-long segment of the thread. It is clear that only the polymeric stress of the Oldroyd-B thread in vacuum is axially uniform in the filament, whose growth in time follows the $1/3De$ exponential law, as shown in figure 10(*e*). The outer fluid phase induces the non-uniformity of $\tau_{zz} - \tau_{rr}$ in the filament of Oldroyd-B fluid, with the minimum stress located near the centre of the filament between the primary droplet at $z = 0$ and the formed secondary droplet at $z = \lambda/2$. Thus the gradient of $\tau_{zz} - \tau_{rr}$ provides a force that tends to push fluid particles in the filament towards the primary or secondary droplet, accelerating the necking of the thread. The Giesekus thread in vacuum has the maximum $\tau_{zz} - \tau_{rr}$ at the midpoint of the filament $z = \lambda/2$. Moreover, this $\tau_{zz} - \tau_{rr}$ at the midpoint grows much faster than the $1/3De$ exponential law, as shown in figure 10(*e*). Away from the midpoint the polymeric stress decreases monotonically and an axially uniform distribution of it can never be built in the filament. In such a case, the filament is most stretched at the midpoint and S_{min} coincides with $S_{\lambda/2}$ all the time ($z_{min} = \lambda/2$), as illustrated in figure 10(*c*). That is, for a Giesekus thread in vacuum, the midpoint of the filament is the place where the thread pinches off. Differently, in the presence of the outer fluid, the maximum $\tau_{zz} - \tau_{rr}$ of the Giesekus thread is located in the neck region connecting the primary droplet to the filament, which suggests that the pinch-off occurs there. Indeed, as shown in figure 10(*c*), its minimum radius z_{min} moves from the midpoint towards the neck at large times and is located there eventually. Away from the neck, $\tau_{zz} - \tau_{rr}$ decreases monotonically, resulting in a negative gradient of polymeric stress in the filament, which tends to push fluid particles towards the primary droplet and accelerate the pinching process. In figure 10(*e*), $\tau_{zz} - \tau_{rr}$ at the midpoint of either Oldroyd-B or Giesekus thread immersed in an outer fluid phase decreases markedly to a minimal value, due to the fact that a secondary droplet is formed at the midpoint.

The extension rate $\dot{\varepsilon} = \partial u / \partial z$ at the midpoint $z = \lambda/2$ is illustrated in figure 10(*f*) for the four cases. It is shown that in the absence of the outer fluid the Giesekus thread has an extension rate much higher than the Oldroyd-B thread whose value is maintained at $2/3De$. Figure 10(*g*) shows the Trouton ratio defined as $\eta_E^i / \eta_0^i = 3\beta + (\tau_{zz} - \tau_{rr})/Oh\dot{\varepsilon}$, where η_E^i is the transient extensional viscosity (Ardekani *et al.* 2010). Only for the Oldroyd-B thread in vacuum does the extensional viscosity grow almost exponentially. In contrast, the extensional viscosity of the Giesekus thread in vacuum stays moderate when pinch-off occurs. In the presence of the outer fluid, the Oldroyd-B or Giesekus thread may experience a sharp increase in the Trouton ratio just before the formation of secondary droplet, as shown in figure 10(*g*). Then, with the formation of a secondary drop at the midpoint, the extensional viscosity there ceases to increase. Instead, the Trouton ratio decreases rapidly and ends up with a small negative value at the moment the secondary droplet is formed (the decrease and the negative values are not shown in the semi-logarithmic plot of figure 10*g*).
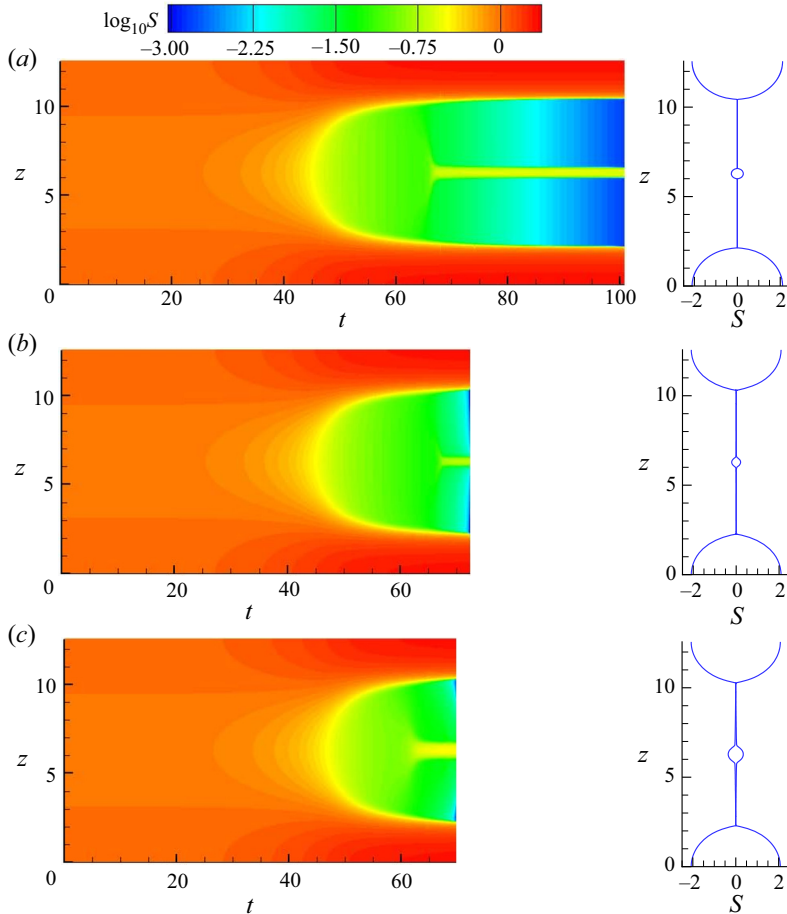
926 A21-18

Figure 11. Space–time diagrams of the deformation of the Oldroyd-B or Giesekus viscoelastic thread and the final profiles for (*a*) $\alpha = 0, m_\eta = 0$, (*b*) $\alpha = 0.005, m_\eta = 0$ and (*c*) $\alpha = 0.005, m_\eta = 0.01$. Here $k = 0.5, Oh = 1.4, \beta = 0.5, De = 3.5, d = 5$.

More space–time diagrams of the evolution of the thread are shown in figure 11, where the axial wavenumber k is fixed at a relatively small value of 0.5. For this relatively long wave, a secondary droplet appears at the midpoint of the Oldroyd-B thread in vacuum, as shown in figure 11(*a*). When α is increased from 0 to 0.005, the secondary droplet at the midpoint is maintained but its size is decreased, as shown in figure 11(*b*). Comparing the space–time diagrams in figures 11(*a*) and 11(*b*), the Giesekus thread necks down much faster than the Oldroyd-B thread. On the other hand, for the Giesekus thread, at the final stages prior to pinch-off, the filament between the primary and secondary droplets becomes non-uniform. In figure 11(*c*), where the viscosity ratio m_η is increased from 0 to 0.01, the non-uniformity of the filament becomes more pronounced, with the aid of the outer fluid, which can be seen from the profile on the right-hand side. Meanwhile, the secondary droplet becomes larger.

4. Conclusion

Based on the slender body theory, a 1-D model is built for a two-phase flow system, in which an infinitely long viscoelastic fluid thread is surrounded by a Newtonian viscous

fluid layer confined in a coaxial cylindrical tube. The viscoelasticity of the inner fluid is described by the Oldroyd-B or Giesekus constitutive equation, and the outer fluid is assumed to be much lighter and much less viscous than the inner fluid. Under such an assumption, the 1-D equations are successfully derived. The effect of the outer viscous fluid phase and the confinement of the tube on the evolution of the beads-on-a-string structure of the viscoelastic thread is examined by numerically solving the nonlinear 1-D equations. Direct simulations and experimental observations will be hopefully carried out in the future to compare with and confirm the 1-D predictions obtained in this work.

In the 1-D model, there are two dimensionless parameters related to the outer fluid or the confinement, i.e. the outer to inner fluid viscosity ratio m_η and the tube to thread radius ratio d. For an Oldroyd-B viscoelastic thread, it is found that the presence of the outer viscous fluid phase may lead to the formation of secondary droplets on the filament between two adjacent primary droplets, even for large wavenumbers. For a fixed wavenumber, as m_η increases, more and more secondary droplets appear in the filament, and meanwhile those existing secondary droplets get larger. The outer viscous fluid exerts a resistance force on the filament, which tends to resist the stretching of the thread. On the other hand, due to the formation of secondary droplets, the capillary and elastic forces are redistributed in the filament, and the polymeric stress loses its uniformity. As a result, the necking of the thread gets slightly faster than in the case of no outer fluid phase. Decreasing the radius ratio d results in an increase in secondary droplet size, but affects little the topological structures of viscoelastic threads.

At sufficiently large wavenumbers, secondary droplets are absent from a Giesekus thread in vacuum, and the thread pinches off at the midpoint of the filament between primary droplets, where the polymeric stress is maximal. In contrast, in the presence of an outer viscous phase, secondary droplets are formed and pinch-off occurs in the neck region connecting the filament to the primary droplet, where the thread is most stressed. Moreover, as m_η increases, the non-uniformity of the filament thickness becomes more and more pronounced.

In addition, a simple linear analysis is executed. The dispersion relations for the 1-D model as well as for the 2-D axisymmetric instability are obtained. It is shown that the mobility factor of the Giesekus model is a secondary factor in linear instability. Increasing m_η or decreasing d may suppress the instability of the viscoelastic thread. The 1-D slender body approximation predicts well the linear instability of the thread at small wavenumbers.

Viscoelasticity influences the linear instability and nonlinear evolution of a viscoelastic thread to a great extent. In this 1-D analysis, the fluid is limited to being of high viscoelasticity (the values of the Ohnesorge and Deborah numbers are relatively large). The present study illuminates just a part of the whole picture. It would be of interest to expand the ranges of the non-dimensional parameters in future 1-D or 2-D numerical simulations.

Declaration of interests. The authors report no conflict of interest.

Author ORCIDs.

Fang Li https://orcid.org/0000-0001-9825-0101;

Dongdong He https://orcid.org/0000-0002-5786-581X.

Appendix A. Derivation of the 1-D model

In the 1-D model, the thread is assumed to be perturbed by a small cosinoidal harmonic at the initial time. Naturally, the radius of the unperturbed thread R is the characteristic length in the radial direction (l_r) and the wavelength of the perturbation $2\pi/k$ is the characteristic length in the axial direction (l_z). Apparently, within the range of the wavenumber k considered, l_r is much smaller than l_z, i.e.

$$l_r = \varepsilon l_z, \tag{A1}$$

where ε is a small parameter. In such a case, the slender body theory can be applied.

The balance of capillary, inertial and viscoelastic forces of the inner fluid gives

$$\rho^i \frac{l_z}{l_t^2} = \eta_0^i \frac{l_z/l_t}{l_z^2} = \frac{\sigma}{l_r} \frac{1}{l_z}. \tag{A2}$$

Using the scales

$$\left. \begin{array}{l} r = l_r \tilde{r}, \; z = l_z \tilde{z}, \; t = l_t \tilde{t}, \; S = l_r \tilde{S}, \; d = l_r \tilde{d}, \; v^i = \frac{l_r}{l_t} \tilde{v}^i, \; v^e = \frac{l_r}{l_t} \tilde{v}^e, \; u^i = \frac{l_z}{l_t} \tilde{u}^i, \; u^e = \frac{l_z}{l_t} \tilde{u}^e, \\[3mm] p^i = \frac{\rho^i l_z^2}{l_t^2} \tilde{p}^i, \; p^e = \frac{\rho^i l_z^2}{l_t^2} \tilde{p}^e, \; \tau_{rr} = \frac{\rho^i l_z^2}{l_t^2} \tilde{\tau}_{rr}, \; \tau_{\theta\theta} = \frac{\rho^i l_z^2}{l_t^2} \tilde{\tau}_{\theta\theta}, \; \tau_{zz} = \frac{\rho^i l_z^2}{l_t^2} \tilde{\tau}_{zz}, \; \tau_{rz} = \frac{\rho^i l_z^3}{l_r l_t^2} \tilde{\tau}_{rz}, \end{array} \right\} \tag{A3}$$

where the tilde denotes the corresponding non-dimensional quantities, and omitting the tildes, one can get the following non-dimensionalized governing equations and boundary conditions.

For the inner viscoelastic fluid:

$$\frac{1}{r} \frac{\partial (r v^i)}{\partial r} + \frac{\partial u^i}{\partial z} = 0, \tag{A4}$$

$$\frac{\partial v^i}{\partial t} + v^i \frac{\partial v^i}{\partial r} + u^i \frac{\partial v^i}{\partial z} = -\frac{1}{\varepsilon^2} \frac{\partial p^i}{\partial r} + \frac{\beta}{\varepsilon^2} \left(\frac{\partial^2 v^i}{\partial r^2} + \frac{1}{r} \frac{\partial v^i}{\partial r} - \frac{v^i}{r^2} \right) + \beta \frac{\partial^2 v^i}{\partial z^2}$$
$$+ \frac{1}{\varepsilon^2} \left(\frac{\partial \tau_{rr}}{\partial r} + \frac{\partial \tau_{rz}}{\partial z} + \frac{\tau_{rr} - \tau_{\theta\theta}}{r} \right), \tag{A5}$$

$$\frac{\partial u^i}{\partial t} + v^i \frac{\partial u^i}{\partial r} + u^i \frac{\partial u^i}{\partial z} = -\frac{\partial p^i}{\partial z} + \frac{\beta}{\varepsilon^2} \left(\frac{\partial^2 u^i}{\partial r^2} + \frac{1}{r} \frac{\partial u^i}{\partial r} \right)$$
$$+ \beta \frac{\partial^2 u^i}{\partial z^2} + \frac{1}{\varepsilon^2} \frac{\partial \tau_{rz}}{\partial r} + \frac{1}{\varepsilon^2} \frac{\tau_{rz}}{r} + \frac{\partial \tau_{zz}}{\partial z}, \tag{A6}$$

$$\tau_{rr} + De \left(\frac{\partial \tau_{rr}}{\partial t} + v^i \frac{\partial \tau_{rr}}{\partial r} + u^i \frac{\partial \tau_{rr}}{\partial z} - 2\tau_{rr} \frac{\partial v^i}{\partial r} - 2\tau_{rz} \frac{\partial v^i}{\partial z} \right)$$
$$+ \frac{\alpha De}{1 - \beta} \left(\tau_{rr}^2 + \frac{1}{\varepsilon^2} \tau_{rz}^2 \right) = 2(1 - \beta) \frac{\partial v^i}{\partial r}, \tag{A7}$$

$$\tau_{\theta\theta} + De \left(\frac{\partial \tau_{\theta\theta}}{\partial t} + v^i \frac{\partial \tau_{\theta\theta}}{\partial r} + u^i \frac{\partial \tau_{\theta\theta}}{\partial z} - 2\tau_{\theta\theta} \frac{v^i}{r} \right) + \frac{\alpha De}{1 - \beta} \tau_{\theta\theta}^2 = 2(1 - \beta) \frac{v^i}{r}, \tag{A8}$$

$$\tau_{zz} + De \left(\frac{\partial \tau_{zz}}{\partial t} + v^i \frac{\partial \tau_{zz}}{\partial r} + u^i \frac{\partial \tau_{zz}}{\partial z} - \frac{2}{\varepsilon^2} \tau_{rz} \frac{\partial u^i}{\partial r} - 2\tau_{zz} \frac{\partial u^i}{\partial z} \right)$$

$$+ \frac{\alpha De}{1 - \beta} (\tau_{zz}^2 + \tau_{rz}^2) = 2(1 - \beta) \frac{\partial u^i}{\partial z}, \tag{A9}$$

$$\tau_{rz} + De \left(\frac{\partial \tau_{rz}}{\partial t} + v^i \frac{\partial \tau_{rz}}{\partial r} + u^i \frac{\partial \tau_{rz}}{\partial z} + \frac{v^i}{r} \tau_{rz} - \tau_{rr} \frac{\partial u^i}{\partial r} - \varepsilon^2 \tau_{zz} \frac{\partial v^i}{\partial z} \right)$$

$$+ \frac{\alpha De}{1 - \beta} (\tau_{rr} + \tau_{zz}) \tau_{rz} = (1 - \beta) \left(\varepsilon^2 \frac{\partial v^i}{\partial z} + \frac{\partial u^i}{\partial r} \right), \tag{A10}$$

where $\tau_{\theta\theta}$ and τ_{rz} are the $\theta\theta$ and rz components of the polymer stress $\boldsymbol{T}_p$, $De = \lambda^i / l_t$ and $\beta = \eta_s^i / \eta_0^i$.

For the outer Newtonian fluid:

$$\frac{1}{r} \frac{\partial (rv^e)}{\partial r} + \frac{\partial u^e}{\partial z} = 0, \tag{A11}$$

$$m_\rho \left(\frac{\partial v^e}{\partial t} + v^e \frac{\partial v^e}{\partial r} + u^e \frac{\partial v^e}{\partial z} \right) = -\frac{1}{\varepsilon^2} \frac{\partial p^e}{\partial r} + m_\eta \left(\frac{1}{\varepsilon^2} \left(\frac{\partial^2 v^e}{\partial r^2} + \frac{1}{r} \frac{\partial v^e}{\partial r} - \frac{v^e}{r^2} \right) + \frac{\partial^2 v^e}{\partial z^2} \right), \tag{A12}$$

$$m_\rho \left(\frac{\partial u^e}{\partial t} + v^e \frac{\partial u^e}{\partial r} + u^e \frac{\partial u^e}{\partial z} \right) = -\frac{\partial p^e}{\partial z} + m_\eta \left(\frac{1}{\varepsilon^2} \left(\frac{\partial^2 u^e}{\partial r^2} + \frac{1}{r} \frac{\partial u^e}{\partial r} \right) + \frac{\partial^2 u^e}{\partial z^2} \right), \tag{A13}$$

where $m_\rho = \rho^e / \rho^i$ and $m_\eta = \eta_0^e / \eta_0^i$.

On the interface $r = S(z, t)$, the normal dynamic balance is

$$p^i = p^e - \frac{2m_\eta}{1 + \varepsilon^2 \left(\frac{\partial S}{\partial z} \right)^2} \left(\frac{\partial v^e}{\partial r} - \frac{\partial S}{\partial z} \left(\frac{\partial v^e}{\partial z} + \frac{\partial u^e}{\partial r} \right) + \left(\frac{\partial S}{\partial z} \right)^2 \frac{\partial u^e}{\partial z} \right)$$

$$+ \frac{2\beta}{1 + \varepsilon^2 \left(\frac{\partial S}{\partial z} \right)^2} \left(\frac{\partial v^i}{\partial r} - \frac{\partial S}{\partial z} \left(\varepsilon^2 \frac{\partial v^i}{\partial z} + \frac{\partial u^i}{\partial r} \right) + \varepsilon^2 \left(\frac{\partial S}{\partial z} \right)^2 \frac{\partial u^i}{\partial z} \right)$$

$$+ \frac{1}{1 + \varepsilon^2 \left(\frac{\partial S}{\partial z} \right)^2} \left(\varepsilon^2 \left(\frac{\partial S}{\partial z} \right)^2 \tau_{zz} - 2 \frac{\partial S}{\partial z} \tau_{rz} + \tau_{rr} \right)$$

$$+ \frac{1}{S \left(1 + \varepsilon^2 \left(\frac{\partial S}{\partial z} \right)^2 \right)^{1/2}} - \frac{\varepsilon^2 \frac{\partial^2 S}{\partial z^2}}{\left(1 + \varepsilon^2 \left(\frac{\partial S}{\partial z} \right)^2 \right)^{3/2}}, \tag{A14}$$

the tangential force balance is

$$\frac{1}{1+\varepsilon^2\left(\frac{\partial S}{\partial z}\right)^2}\left(2\beta\varepsilon^2\frac{\partial S}{\partial z}\left(\frac{\partial v^i}{\partial r}-\frac{\partial u^i}{\partial z}\right)+\beta\left(1-\varepsilon^2\left(\frac{\partial S}{\partial z}\right)^2\right)\left(\varepsilon^2\frac{\partial v^i}{\partial z}+\frac{\partial u^i}{\partial r}\right)\right)$$

$$+\frac{1}{1+\varepsilon^2\left(\frac{\partial S}{\partial z}\right)^2}\left(\varepsilon^2\frac{\partial S}{\partial z}(\tau_{rr}-\tau_{zz})+\left(1-\varepsilon^2\left(\frac{\partial S}{\partial z}\right)^2\right)\tau_{rz}\right)$$

$$=\frac{1}{1+\varepsilon^2\left(\frac{\partial S}{\partial z}\right)^2}\left(2m_\eta\frac{\partial S}{\partial z}\varepsilon^2\left(\frac{\partial v^e}{\partial r}-\frac{\partial u^e}{\partial z}\right)\right.$$

$$\left.+m_\eta\left(1-\varepsilon^2\left(\frac{\partial S}{\partial z}\right)^2\right)\left(\varepsilon^2\frac{\partial v^e}{\partial z}+\frac{\partial u^e}{\partial r}\right)\right),\tag{A15}$$

the kinematic boundary condition is

$$v^i=\frac{\partial S}{\partial t}+u^i\frac{\partial S}{\partial z}\tag{A16}$$

and the continuity of velocity requires

$$u^i=u^e\quad\text{and}\quad v^i=v^e.\tag{A17a,b}$$

The boundary conditions on the tube wall are

$$u^e(d,z,t)=v^e(d,z,t)=0.\tag{A18}$$

Now we expand the quantities into Taylor series of εr. For the inner viscoelastic thread:

$$u^i(r,z,t)=u^i_0(z,t)+u^i_2(z,t)\frac{(\varepsilon r)^2}{2}+\cdots,\tag{A19}$$

$$v^i(r,z,t)=-\frac{r}{2}\frac{\partial u^i_0}{\partial z}-\frac{\varepsilon^2 r^3}{8}\frac{\partial u^i_2(z,t)}{\partial z}+\cdots,\tag{A20}$$

$$p^i(r,z,t)=p^i_0(z,t)+p^i_2(z,t)(\varepsilon r)^2+\cdots,\tag{A21}$$

$$\tau_{rr}(r,z,t)=\tau_{rr0}(z,t)+\tau_{rr2}(z,t)(\varepsilon r)^2+\cdots,\tag{A22}$$

$$\tau_{zz}(r,z,t)=\tau_{zz0}(z,t)+\tau_{zz2}(z,t)(\varepsilon r)^2+\cdots,\tag{A23}$$

$$\tau_{\theta\theta}(r,z,t)=\tau_{\theta\theta0}(z,t)+\tau_{\theta\theta2}(z,t)(\varepsilon r)^2+\cdots,\tag{A24}$$

$$r\tau_{rz}(r,z,t)=\tau_{rz0}(z,t)+\tau_{rz2}(z,t)(\varepsilon r)^2+\cdots.\tag{A25}$$

For the outer Newtonian fluid:

$$u^e(r,z,t)=u^e_0(r,z,t)+u^e_2(r,z,t)\varepsilon^2+\cdots,\tag{A26}$$

$$v^e(r,z,t)=v^e_0(r,z,t)+v^e_2(r,z,t)\varepsilon^2+\cdots,\tag{A27}$$

$$p^e(r,z,t)=p^e_0(r,z,t)+p^e_2(r,z,t)\varepsilon^2+\cdots.\tag{A28}$$

Substituting the expansions (A19)–(A28) into the kinematic condition (A16), the leading order yields

$$v_0^i(S, z, t) = \frac{\partial S}{\partial t} + u_0^i \frac{\partial S}{\partial z} = -\frac{S}{2} \frac{\partial u_0^i}{\partial z}. \tag{A29}$$

This gives

$$\frac{\partial(S^2)}{\partial t} + \frac{\partial(S^2 u_0^i)}{\partial z} = 0. \tag{A30}$$

Substituting the expansions into (A4)–(A10), one has $\tau_{rz0} = 0$, $\tau_{rr0} = \tau_{\theta\theta 0}$ and

$$\frac{\partial u_0^i}{\partial t} + u_0^i \frac{\partial u_0^i}{\partial z} = -\frac{\partial p_0^i}{\partial z} + \beta \left(2u_2^i + \frac{\partial^2 u_0^i}{\partial z^2} \right) + 2\tau_{rz2} + \frac{\partial \tau_{zz0}}{\partial z}, \tag{A31}$$

$$\tau_{rr0} + De \left(\frac{\partial \tau_{rr0}}{\partial t} + u_0^i \frac{\partial \tau_{rr0}}{\partial z} + \tau_{rr0} \frac{\partial u_0^i}{\partial z} \right) + \frac{\alpha De}{1 - \beta} \tau_{rr0}^2 = -(1 - \beta) \frac{\partial u_0^i}{\partial z}, \tag{A32}$$

$$\tau_{zz0} + De \left(\frac{\partial \tau_{zz0}}{\partial t} + u_0^i \frac{\partial \tau_{zz0}}{\partial z} - 2\tau_{zz0} \frac{\partial u_0^i}{\partial z} \right) + \frac{\alpha De}{1 - \beta} \tau_{zz0}^2 = 2(1 - \beta) \frac{\partial u_0^i}{\partial z}, \tag{A33}$$

$$\tau_{\theta\theta 0} + De \left(\frac{\partial \tau_{\theta\theta 0}}{\partial t} + u_0^i \frac{\partial \tau_{\theta\theta 0}}{\partial z} - 2\tau_{\theta\theta 0} \frac{\partial u_0^i}{\partial z} \right) + \frac{\alpha De}{1 - \beta} \tau_{\theta\theta 0}^2 = -(1 - \beta) \frac{\partial u_0^i}{\partial z}, \tag{A34}$$

$$\tau_{rz2} + De \left(\frac{\partial \tau_{rz2}}{\partial t} - \tau_{rz2} \frac{\partial u_0^i}{\partial z} + u_0^i \frac{\partial \tau_{rz2}}{\partial z} - \tau_{rr0} u_2^i + \frac{1}{2} \tau_{zz0} \frac{\partial^2 u_0^i}{\partial z^2} \right)$$

$$+ \frac{\alpha De}{1 - \beta} (\tau_{rr0} + \tau_{zz0}) \tau_{rz2} = (1 - \beta) \left(u_2^i - \frac{1}{2} \frac{\partial^2 u_0^i}{\partial z^2} \right). \tag{A35}$$

Assume that $m_\rho = \rho^e / \rho^i \sim O(\varepsilon)$ and $m_\eta = \eta_0^e / \eta_0^i \sim O(\varepsilon^2) = \lambda_0 \varepsilon^2$, where λ_0 is a constant of $O(1)$. Equation (A12) at $O(1/\varepsilon^2)$ gives

$$\frac{\partial p_0^e}{\partial r} = 0, \tag{A36}$$

which implies that $p_0^e = p_0^e(z, t)$. Equation (A13) at $O(1)$ gives

$$-\frac{\partial p_0^e}{\partial z} + \lambda_0 \frac{1}{r} \frac{\partial \left(r \dfrac{\partial u^e}{\partial r} \right)}{\partial r} = 0, \tag{A37}$$

and then we obtain

$$u_0^e = \frac{r^2}{4\lambda_0} \frac{\partial p_0^e}{\partial z} + A(z, t) \ln r + B(z, t), \tag{A38}$$

where $A(z, t)$ and $B(z, t)$ are functions of z and t to be determined.

From (A11) and (A38), one can obtain

$$v_0^e = -\frac{r^3}{16\lambda_0}\frac{\partial^2 p_0^e}{\partial z^2} + \frac{\partial A}{\partial z}\left(\frac{r}{4} - \frac{r\ln r}{2}\right) - \frac{\partial B}{\partial z}\frac{r}{2} + \frac{C}{r}. \tag{A39}$$

From (A18), one has

$$B = -\frac{d^2}{4\lambda_0}\frac{\partial p_0^e}{\partial z} - A\ln d, \tag{A40}$$

$$C = \frac{d^4}{16\lambda_0}\frac{\partial^2 p_0^e}{\partial z^2} - \frac{\partial A}{\partial z}\left(\frac{d^2}{4} - \frac{d^2\ln d}{2}\right) + \frac{\partial B}{\partial z}\frac{d^2}{2}. \tag{A41}$$

Therefore, (A 17) yields

$$u_0^e = \frac{r^2 - d^2}{4\lambda_0}\frac{\partial p_0^e}{\partial z} + A\ln\frac{r}{d}, \tag{A42}$$

$$v_0^e = -\frac{1}{\lambda_0}\left(\frac{(r^2 - d^2)^2}{16r}\frac{\partial^2 p_0^e}{\partial z^2} + \lambda_0\frac{2r^2\ln\frac{r}{d} + d^2 - r^2}{4r}\frac{\partial A}{\partial z}\right). \tag{A43}$$

Thus

$$u_0^i(z,t) = u_0^i|_{r=S} = u_0^e(S,z,t) = \frac{S^2 - d^2}{4\lambda_0}\frac{\partial p_0^e}{\partial z} + A\ln\frac{S}{d}. \tag{A44}$$

From (A4), one has

$$v_0^i = -\frac{r}{2}\frac{\partial u_0^i}{\partial z}. \tag{A45}$$

Thus

$$v_0^i(S,z,t) = \left(-\frac{r}{2}\frac{\partial u_0^i}{\partial z}\right)\bigg|_{r=S} = -\frac{S}{2}\left(\frac{S^2 - d^2}{4\lambda_0}\frac{\partial p_0^e}{\partial z} + A\ln\frac{S}{d}\right)_z. \tag{A46}$$

On the other hand,

$$v_0^e(S,z,t) = -\frac{1}{\lambda_0}\left(\frac{(S^2 - d^2)^2}{16r}\frac{\partial^2 p_0^e}{\partial z^2} + \lambda_0\frac{2S^2\ln\frac{S}{d} + d^2 - S^2}{4S}\frac{\partial A}{\partial z}\right). \tag{A47}$$

Equations (A45) and (A47) together with (A 17) yield

$$A = -\frac{S^2 + d^2}{4\lambda_0}\frac{\partial p_2^e}{\partial z} + \frac{f(t)}{(S^2 - d^2)\lambda_0}, \tag{A48}$$

where $f(t)$ is an arbitrary function of time t.

Thus, (A44) further gives

$$\frac{\partial p_2^e}{\partial z} = \frac{\lambda_0 u_0^i - \dfrac{f(t)}{S^2 - d^2} \ln \dfrac{S}{d}}{\dfrac{S^2 - d^2}{4} - \dfrac{S^2 + d^2}{4} \ln \dfrac{S}{d}}. \tag{A49}$$

The normal condition (A14) at $O(1)$ together with (A19) and (A45) yields

$$p_0^i = p_0^e - \beta \frac{\partial u_0^i}{\partial z} + \tau_{rr0} + \hat{\kappa} \tag{A50}$$

and

$$\frac{\partial p_0^i}{\partial z} = \frac{\partial p_0^e}{\partial z} - \beta \frac{\partial^2 u_0^i}{\partial z^2} + \frac{\partial \tau_{rr0}}{\partial z} + \frac{\partial \hat{\kappa}}{\partial z}, \tag{A51}$$

where

$$\hat{\kappa} = \frac{1}{S \left(1 + \varepsilon^2 \left(\dfrac{\partial S}{\partial z}\right)^2\right)} - \frac{\varepsilon^2 \dfrac{\partial^2 S}{\partial z^2}}{\left(1 + \varepsilon^2 \left(\dfrac{\partial S}{\partial z}\right)^2\right)^{3/2}}. \tag{A52}$$

The tangential condition (A15) at $O(\varepsilon^2)$ together with (A19), (A42) and (A45) gives

$$-3\beta \frac{\partial S}{\partial z} \frac{\partial u_0^i}{\partial z} + \beta \frac{\partial v_0^i}{\partial z} + S \left(\beta u_2^i + \tau_{rz2}\right) + \frac{\partial S}{\partial z} (\tau_{rr0} - \tau_{zz0}) = \frac{S^2 - d^2}{4S} \frac{\partial p_0^e}{\partial z} + \frac{f(t)}{S(S^2 - d^2)}. \tag{A53}$$

Equation (A6) at O(1) gives

$$\frac{\partial u_0^i}{\partial t} + u_0^i \frac{\partial u_0^i}{\partial z} = -\frac{\partial p_0^i}{\partial z} + 2 \left(\beta u_2^i + \tau_{rz2}\right) + \beta \frac{\partial^2 u_0^i}{\partial z^2} + \frac{\partial \tau_{zz0}}{\partial z}. \tag{A54}$$

Using (A49), (A51), (A53) and (A54), one can obtain

$$\frac{\partial u_0^i}{\partial t} + u_0^i \frac{\partial u_0^i}{\partial z} = \frac{\beta}{S^2} \frac{\partial \left(3S^2 \dfrac{\partial u_0^i}{\partial z}\right)}{\partial z} + \frac{1}{S^2} \frac{\partial \left(S^2 (\tau_{zz0} - \tau_{rr0})\right)}{\partial z} - \frac{\partial \hat{\kappa}}{\partial z} - \frac{2}{S^2} \left(\lambda_0 u_0^i - \frac{f(t)}{S^2 + d^2}\right) G(S, d), \tag{A55}$$

where

$$G(S, d) = \frac{S^2 + d^2}{S^2 - d^2 - (S^2 + d^2) \ln \dfrac{S}{d}}. \tag{A56}$$

Equations (A30), (A32), (A33) and (A55) constitute the 1-D model. For brevity we drop the superscript i and the subscript 0.

Note that in this problem the shape of the stretched thread is spatially periodic in the z direction. Being a cosinoidal harmonic perturbation imposed on the thread at the initial time (Wang 2013), one has

$$f(t) = \frac{\int_{-\lambda/2}^{\lambda/2} S^2 \left(\frac{\partial u^i}{\partial t} + u^i \frac{\partial u^i}{\partial z}\right) dz + 2\lambda_0 \int_{-\lambda/2}^{\lambda/2} u^i G(S, d) \, dz}{\int_{-\lambda/2}^{\lambda/2} \frac{2G(S, d)}{S^2 + d^2} \, dz} = 0, \qquad (A57)$$

where $\lambda = 2\pi/kR$ is the dimensionless wavelength of the perturbation.

Now one can write the above 1-D equations in the following dimensional form:

$$\frac{\partial(S^2)}{\partial t} + \frac{\partial(S^2 u^i)}{\partial z} = 0, \qquad (A58)$$

$$\rho^i \left(\frac{\partial u^i}{\partial t} + u^i \frac{\partial u^i}{\partial z}\right) = \frac{3\eta_s^i}{S^2} \frac{\partial \left(S^2 \frac{\partial u^i}{\partial z}\right)}{\partial z} + \frac{1}{S^2} \frac{\partial(S^2(\tau_{zz} - \tau_{rr}))}{\partial z} - \sigma \frac{\partial \kappa}{\partial z} - \frac{2}{S^2} \eta_0^e u^i G(S, R_0), \qquad (A59)$$

$$\tau_{zz} + \lambda^i \left(\frac{\partial \tau_{zz}}{\partial t} + u^i \frac{\partial \tau_{zz}}{\partial z} - 2\tau_{zz} \frac{\partial u^i}{\partial z}\right) + \frac{\alpha \lambda^i}{\eta_p^i} \tau_{zz}^2 = 2\eta_p^i \frac{\partial u^i}{\partial z}, \qquad (A60)$$

$$\tau_{rr} + \lambda^i \left(\frac{\partial \tau_{rr}}{\partial t} + u^i \frac{\partial \tau_{rr}}{\partial z} + \tau_{rr} \frac{\partial u^i}{\partial z}\right) + \frac{\alpha \lambda^i}{\eta_p^i} \tau_{rr}^2 = -\eta_p^i \frac{\partial u^i}{\partial z}, \qquad (A61)$$

where

$$G(S, R_0) = \frac{S^2 + R_0^2}{S^2 - R_0^2 - (S^2 + R_0^2) \ln \frac{S}{R_0}}, \quad \kappa = \frac{1}{S \left(1 + \left(\frac{\partial S}{\partial z}\right)^2\right)^{1/2}} - \frac{\frac{\partial^2 S}{\partial z^2}}{\left(1 + \left(\frac{\partial S}{\partial z}\right)^2\right)^{3/2}}. \qquad (A62)$$

Appendix B. Linear stability analysis of the 2-D axisymmetric model

In this Appendix, we derive the dispersion relation for the 2-D axisymmetric linear stability from (2.1)–(2.15). The basic state of this model is

$$\bar{u}^i = \bar{v}^i = \bar{u}^e = \bar{v}^e = 0, \quad \bar{p}^i - \bar{p}^e = \frac{\sigma}{R}, \quad \bar{\tau}_{zz} = \bar{\tau}_{rr} = \bar{\tau}_{rz} = \bar{\tau}_{\theta\theta} = 0. \qquad (B1a\text{--}c)$$

Following the normal mode method, the quantities after being perturbed are decomposed into

$$
\left.\begin{aligned}
u^i &= \hat{u}^i \exp(\omega t + jkz) + \text{c.c.}, \\
v^i &= \hat{u}^i \exp(\omega t + jkz) + \text{c.c.}, \\
p^i &= \bar{p}^i + \hat{p}^i \exp(\omega t + jkz) + \text{c.c.}, \\
\tau_{zz} &= \hat{\tau}_{zz} \exp(\omega t + jkz) + \text{c.c.}, \\
\tau_{rr} &= \hat{\tau}_{rr} \exp(\omega t + jkz) + \text{c.c.}, \\
\tau_{rz} &= \hat{\tau}_{zz} \exp(\omega t + jkz) + \text{c.c.}, \\
\tau_{\theta\theta} &= \hat{\tau}_{\theta\theta} \exp(\omega t + jkz) + \text{c.c.}, \\
u^e &= \hat{u}^e \exp(\omega t + jkz) + \text{c.c.}, \\
v^e &= \hat{u}^e \exp(\omega t + jkz) + \text{c.c.}, \\
p^e &= \bar{p}^e + \hat{p}^e \exp(\omega t + jkz) + \text{c.c.},
\end{aligned}\right\}
\tag{B2}
$$

where the hat indicates the amplitude of the perturbation.

Substituting the above decompositions into (2.1)–(2.8), performing linearization and introducing the stream functions $\psi^i(r, z, t) = \hat{\psi}^i(r) \exp(\omega t + jkz) + \text{c.c.}$ and $\psi^e(r, z, t) = \hat{\psi}^e(r) \exp(\omega t + jkz) + \text{c.c.}$, one can obtain

$$
\left.\begin{aligned}
\hat{\psi}^i &= rI_1(kr)A_1^i + rI_1(k_ir)A_2^i, \\
\hat{u}^i &= -\frac{1}{r}\hat{\psi}_r^i = -kI_0(kr)A_1^i - k_iI_0(k_ir)A_2^i, \\
\hat{v}^i &= \frac{jk\hat{\psi}^i}{r} = jk(I_1(kr)A_1^i + I_1(k_ir)A_2^i), \\
\hat{p}^i &= -j\omega\rho^i I_0(kr)A_1^i, \\
\hat{\tau}_{zz} &= 2\bar{\eta}_0^i jk\hat{u}^i, \\
\hat{\tau}_{rr} &= 2\bar{\eta}_0^i \frac{d\hat{v}^i}{dr}, \\
\hat{\tau}_{rz} &= \bar{\eta}_0^i \left(\frac{d\hat{u}^i}{dr} + jk\hat{v}^i\right), \\
\hat{\tau}_{\theta\theta} &= 2\bar{\eta}_0^i \frac{\hat{v}^i}{r}, \\
\hat{\psi}^e &= rI_1(kr)A_1^e + rK_1(kr)B_2^e + rI_1(k_er)A_2^e + rK_1(k_er)B_2^e, \\
\hat{u}^e &= -\frac{1}{r}\hat{\psi}_r^e = -kI_0(kr)A_1^e + kK_0(kr)B_1^e - k_eI_0(k_er)A_2^e + k_eK_0(k_er)B_2^e, \\
\hat{v}^e &= \frac{jk\hat{\psi}^e}{r} = jk(I_1(kr)A_1^e + K_1(kr)B_1^e + I_1(k_er)A_2^e + K_1(k_er)B_2^e), \\
\hat{p}^e &= -j\omega\rho^e I_0(kr)A_1^e + j\omega\rho^e K_0(kr)B_1^e,
\end{aligned}\right\}
\tag{B3}
$$

where A_1^i, A_2^i, A_1^e, A_2^e, B_1^e, B_2^e are constants to be determined and

$$
k_i = \sqrt{k^2 + \frac{\omega\rho^i(1 + \omega\lambda^i)}{\eta_0^i(1 + \omega\beta\lambda^i)}}, \quad k_e = \sqrt{k^2 + \frac{\omega\rho^e}{\eta_0^e}} \quad \text{and} \quad \bar{\eta}_0^i = \eta_0^i \frac{1 + \omega\beta\lambda^i}{1 + \omega\lambda^i}.
\tag{B4}
$$

Substituting the above solutions into the boundary conditions (2.9)–(2.15) and linearizing them, one obtains a system of equations for the unknown constants A_1^i, A_2^i, A_1^e, A_2^e, B_1^e and B_2^e. In order to have non-trivial solutions, the determinant of the corresponding coefficient matrix must be zero, which yields the non-dimensional dispersion relation (3.8).

REFERENCES

ANNA, S.L. & MCKINLEY, G.H. 2001 Elasto-capillary thinning and breakup of model elastic liquids. *J. Rheol.* **45**, 115–138.

ARDEKANI, A.M., SHARMA, V. & MCKINLEY, G.H. 2010 Dynamics of bead formation, filament thinning and breakup in weakly viscoelastic jets. *J. Fluid Mech.* **665**, 46–56.

ARRATIA, P.E., CRAMER, L.-A., GOLLUB, J.P. & BURIAN, D.J. 2009 The effects of polymer molecular weight on filament thinning and drop breakup in microchannels. *New J. Phys.* **11**, 115006.

BHAT, P.P., APPATHURAI, S., HARRIS, M.T. & BASARAN, O.A. 2012 On self-similarity in the drop-filament corner region formed during pinch-off of viscoelastic fluid threads. *Phys. Fluids* **24**, 083101.

BHAT, P.P., APPATHURAI, S., HARRIS, M.T., PASQUALI, M., MCKINLEY, G.H. & BASARAN, O.A. 2010 Formation of beads-on-a-string structures during break-up of viscoelastic filaments. *Nat. Phys.* **6**, 625–631.

BIRJANDI, A.K., NOROUZI, M. & KAYHANI, M.H. 2017 A numerical study on drop formation of viscoelastic liquids using a nonlinear constitutive equation. *Meccanica* **52**, 3593–3613.

BOUSFIELD, D.W., KEUNINGS, R., MARRUCCI, G. & DENN, M.M. 1986 Nonlinear analysis of the surface tension driven breakup of viscoelastic filaments. *J. Non-Newtonian Fluid Mech.* **1986**, 79–97.

CABEZAS, M.G., REBOLLO-MUÑOZ, N., RUBIO, M., HERRADA, M.A. & MONTANERO, J.M. 2021 Global stability analysis of axisymmetric liquid–liquid flow focusing. *J. Fluid Mech.* **909**, A10.

CHANG, H.-C., DEMEKHIN, E.A. & KALAIDIN, E. 1999 Iterated stretching of viscoelastic jets. *Phys. Fluids* **11**, 1717–1737.

CHRISTANTI, Y. & WALKER, L.M. 2001 Surface tension driven jet break up of strain-hardening polymer solutions. *J. Non-Newtonian Fluid Mech.* **100**, 9–26.

CLASEN, C., EGGERS, J., FONTELOS, M.A., LI, J. & MCKINLEY, G.H. 2006*a* The beads-on-string structure of viscoelastic threads. *J. Fluid Mech.* **556**, 283–308.

CLASEN, C., PLOG, J.P., KULICKE, W.-M., MACOSKO, M., SCRIVEN, L.E., VERANI, M. & MCKINLEY, G.H. 2006*b* How dilute are dilute solutions in extensional flows? *J. Rheol.* **50**, 849–881.

DEBLAIS, A., HERRADA, M.A., EGGERS, J. & BONN, D. 2020 Self-similarity in the breakup of very dilute viscoelastic solutions. *J. Fluid Mech.* **904**, R2.

DEBLAIS, A., VELIKOV, K.P. & BONN, D. 2018 Pearling instabilities of a viscoelastic thread. *Phys. Rev. Lett.* **120**, 194501.

DU, W., FU, T., ZHANG, Q., ZHU, C., MA, Y. & LI, H.Z. 2016 Breakup dynamics for droplet formation in a flow-focusing device: Rupture position of viscoelastic thread from matrix. *Chem. Engng Sci.* **153**, 255–269.

EGGERS, J. 2014 Instability of a polymeric thread. *Phys. Fluids* **26**, 033106.

EGGERS, J. & DUPONT, T.F. 1994 Drop formation in a one-dimensional approximation of the Navier–Stokes equation. *J. Fluid Mech.* **262**, 205–221.

EGGERS, J., HERRADA, M.A. & SNOEIJER, J.H. 2020 Self-similar breakup of polymeric threads as described by the Oldroyd-B model. *J. Fluid Mech.* **887**, A19.

EGGERS, J. & VILLERMAUX, E. 2008 Physics of liquid jets. *Rep. Prog. Phys.* **71**, 036601.

ENTOV, V.M. & HINCH, E.J. 1997 Effect of a spectrum of relaxation times on the capillary thinning of a filament of elastic liquid. *J. Non-Newtonian Fluid Mech.* **72**, 31–53.

FENG, J.J. 2003 Stretching of a straight electrically charged viscoelastic jet. *J. Non-Newtonian Fluid Mech.* **116**, 55–70.

FIGUEIREDO, R.A., OISHI, C.M., AFONSO, A.M. & ALVES, M.A. 2020 Numerical study on micro-scale extensional viscoelastic flows. *J. Non-Newtonian Fluid Mech.* **276**, 104219.

FONTELOS, M.A. & LI, J. 2004 On the evolution and rupture of filaments in Giesekus and FENE models. *J. Non-Newtonian Fluid Mech.* **118**, 1–16.

GOLDIN, M., YERUSHALMI, J., PFEFFER, R. & SHINNAR, R. 1969 Breakup of a laminar capillary jet of a viscoelastic fluid. *J. Fluid Mech.* **38**, 689–711.

GUNAWAN, A.Y., MOLENAAR, J. & WAN DE VEN, A.A.F. 2005 Temporal stability of a viscoelastic immersed thread in a confined region. *J. Non-Newtonian Fluid Mech.* **126**, 83–92.

HOMMA, S., KOGA, J., MATSUMOTO, S., SONG, M. & TRYGGVASON, G. 2006 Breakup mode of an axisymmetric liquid jet injected into another immiscible liquid. *Chem. Engng Sci.* **61**, 3986–3996.

KAMAT, P.M., WAGONER, B.W., THETE, S.S. & BASARAN, O.A. 2018 Role of Marangoni stress during breakup of surfactant-covered liquid threads: reduced rates of thinning and microthread cascades. *Phys. Rev. Fluids* **3**, 043602.

KESHAVARZ, B., SHARMA, V., HOUZE, E.C., KOERNER, M.R., MOORE, J.R., COTTS, P.M., THRELFALL-HOLMES, P. & MCKINLEY, G.H. 2015 Studying the effects of elongational properties on atomization of weakly viscoelastic solutions using Rayleigh Ohnesorge Jetting Extensional Rheometry (ROJER). *J. Non-Newtonian Fluid Mech.* **222**, 171–189.

KULICHIKHIN, V.G., MALKIN, A.Y., SEMAKOV, A.V., SKVORTSOV, I.Y. & ARINSTEIN, A. 2014 Liquid filament instability due to stretch-induced phase separation in polymer solutions. *Eur. Phys. J.* E **37**, 10.

LEE, E.R. 2003 *Microdrop Generation*. CRC Press.

LI, F., KE, S.-Y., YIN, X.-Y. & YIN, X.-Z. 2019 Effect of finite conductivity on the nonlinear behaviour of an electrically charged viscoelastic liquid jet. *J. Fluid Mech.* **874**, 5–37.

LI, F., YIN, X.-Y. & YIN, X.-Z. 2017*a* Oscillation of satellite droplets in an Oldroyd-B viscoelastic liquid jet. *Phys. Rev. Fluids* **2**, 013602.

LI, F., YIN, X.-Y. & YIN, X.-Z. 2017*b* Transition from a beads-on-string to a spike structure in an electrified viscoelastic jet. *Phys. Fluids* **29**, 023106.

LISTER, J.R. & STONE, H.A. 1998 Capillary breakup of a viscous thread surrounded by another viscous fluid. *Phys. Fluids* **10**, 2758–2764.

MALKIN, A.Y., ARINSTEIN, A. & KULICHIKHIN, V.G. 2014 Polymer extension flows and instabilities. *Prog. Polym. Sci.* **39**, 959–978.

MATHUES, W., FORMENTI, S., MCLLROY, C., HARLEN, O.G. & CLASEN, C. 2018 CaBER vs ROJER-different time scales for the thinning of a weakly elastic jet. *J. Rheol.* **62**, 1135–1153.

MIDDLEMAN, S. 1965 Stability of a viscoelastic jet. *Chem. Engng Sci.* **20**, 1037–1040.

MONTANERO, J.M. & GAÑÁN-CALVO, A.M. 2020 Dripping, jetting and tip streaming. *Rep. Prog. Phys.* **83**, 097001.

OLIVEIRA, M.S.N., YEH, R. & MCKINLEY, G.H. 2006 Iterated stretching, extensional rheology and formation of beads-on-a-string structures in polymer solutions. *J. Non-Newtonian Fluid Mech.* **137**, 137–148.

PINGULKAR, H., PEIXINHO, J. & CRUMEYROLLE, O. 2020 Drop dynamics of viscoelastic filaments. *Phys. Rev. Fluids* **5**, 011301.

SATTLER, R., GIER, S., EGGERS, J. & WAGNER, C. 2012 The final stages of capillary break-up of polymer solutions. *Phys. Fluids* **24**, 023101.

SATTLER, R., WAGNER, C. & EGGERS, J. 2008 Blistering pattern and formation of nanofibers in capillary thinning of polymer solutions. *Phys. Rev. Lett.* **100**, 164502.

SIEROU, A. & LISTER, J.R. 2003 Self-similar solutions for viscous capillary pinch-off. *J. Fluid Mech.* **497**, 381–403.

SNOEIJER, J.H., PANDEY, A., HERRADA, M.A. & EGGERS, J. 2020 The relationship between viscoelasticity and elasticity. *Proc. R. Soc.* A **476**, 20200419.

SOUSA, P.C., VEGA, E.J., SOUSA, R.G., MONTANERO, J.M. & ALVES, M.A. 2017 Measurement of relaxation times in extensional flow of weakly viscoelastic polymer solutions. *Rheol. Acta* **56**, 11–20.

TEMBELY, M., VADILLO, D., MACKLEY, M.R. & SOUCEMARIANADIN, A. 2012 The matching of a one-dimensional numerical simulation and experiment results for low viscosity Newtonian and non-Newtonian fluids during fast filament stretching and subsequent break-up. *J. Rheol.* **56**, 159–183.

TJAHJADI, M., STONE, H.A. & OTTINO, J.M. 1992 Satellite and subsatellite formation in capillary breakup. *J. Fluid Mech.* **243**, 297–317.

TURKOZ, E., LOPEZ-HERRERA, J.M., EGGERS, J., ARNOLD, C.B. & DEIKE, L. 2018*a* Axisymmetric simulation of viscoelastic filament thinning with the Oldroyd-B model. *J. Fluid Mech.* **851**, R2.

TURKOZ, E., PERAZZO, A., KIM, H., STONE, H.A. & ARNOLD, C.B. 2018*b* Impulsively induced jets from viscoelastic films for high-resolution printing. *Phys. Rev. Lett.* **120**, 074501.

VADILLO, D.C., TEMBEYLY, M., MORRISON, N.F., HARLEN, O.G., MACKLEY, M.R. & SOUCEMARIANADIN, A. 2012 The matching of polymer solution fast filament stretching, relaxation, and break up experimental results with 1D and 2D numerical viscoelastic simulation. *J. Rheol.* **56**, 1491–1516.

WAGNER, C., BOUROUIBA, L. & MCKINLEY, G.H. 2015 An analytic solution for capillary thinning and breakup of FENE-P fluids. *J. Non-Newtonian Fluid Mech.* **218**, 53–61.

WANG, Q. 2013 Capillary instability of a viscous liquid thread in a cylindrical tube. *Phys. Fluids* **25**, 112104.

XIE, L., JIA, B., CUI, X., YANG, L. & FU, Q. 2019 Effects of spatially decaying elastic tension on the instability of viscoelastic jets. *Phys. Fluids* **31**, 123107.

ZHAO, C.X. & MIDDELBERG, A.P.J. 2011 Two-phase microfluidic flows. *Chem. Engng Sci.* **66**, 1394–1411.